

The Influence of Solar System Oscillation on the Variability of the Total Solar Irradiance

Harald Yndestad*

Norwegian University of Science and Technology Aalesund, 6025 Aalesund, Norway

Jan-Erik Solheim^{1,*}

Department of Physics and Technology UiT The Arctic University of Norway, 9037 Tromsø, Norway

Abstract

The total solar irradiation (TSI) is the primary quantity of energy that is provided to the Earth. The properties of the TSI variability are critical for understanding the cause of the irradiation variability and its expected influence on climate variations. A deterministic property of TSI variability can provide information about future irradiation variability and expected long-term climate variation, whereas the non-deterministic variability can only explain the past. This study of solar variability is based on an analysis of the TSI data series from 1700 and 1000 A.D., a sunspot data series from 1611, and a solar orbit data series from 1000. The study is based on a wavelet spectrum analysis. First the TSI data series are transformed into a wavelet spectrum. Then the wavelet spectrum is transformed into an autocorrelation spectrum, to identify stationary, subharmonic and coincidence periods in the TSI variability.

The results indicate that the TSI and sunspot data series have periodic cycles that is correlated to the solar position oscillation and controlled by gravity variations from the large planets Jupiter, Saturn, Uranus and Neptune and the solar dynamo. A possible explanation is forced oscillation gravity between the

*Corresponding author

Email address: Harald.Yndestad@ntnu.no (Harald Yndestad)

¹Retired, Address now: Wilh. Wilhemsens v 71, 1362 Hosle, Norway

large planets and the solar dynamo. The major solar variability is controlled by the 12-year Jupiter period and the 84-year Uranus period. The TSI data series from 1700 has a direct relation to the 84-year Uranus period with subharmonics. The phase lag between the solar position oscillation and this TSI oscillation is estimated to about 0.15π (rad/year) for the dominating 84-year period, and is phase locked to the perihel state of Uranus.

The long TSI data series from 1000 has stationary periods of approximately 125 years and 210 years, which are controlled by the same stationary period of 84 year. The minimum of the 125 year period coincide with the time Uranus perihel. The 125-year and the 210-year period subsequently produce a new set of subharmonic periods. The sunspot data series from 1611 has a stationary 12-year Jupiter period and a stationary period of approximately 210 years, which are controlled by a $5/2$ resonance to the 84-year Uranus period. The study confirms that the 12-year Jupiter period and the 210-year de Vries/Suess period have coincidence periods in TSI and sunspot variability. The phase lag between the solar position oscillation and TSI and sunspot oscillation is estimated to about 0.7π (rad/year) for the dominating 210-year period.

A model of the stationary periods in TSI and sunspot variability confirms the results by a close relation to known long solar minimum periods since 1000 and a modern maximum period from 1940 to 2015. The model computes a new Dalton sunspot minimum from approximately 2025 to 2050 and a new Dalton period TSI minimum from approximately 2040 to 2065.

Keywords:

solar oscillation, solar irradiation oscillation, wavelet analysis, grand minima

1. Introduction

The total solar irradiation (TSI) is the primary source of energy that is provided to the Earth's climate system. A variation in the TSI irradiation will contribute to a natural climate variation on the Earth. The variability of the irradiation from the Sun was approximately 0.3% over the last 300 years

(Scafetta & Willson, 2014). A better understanding of the TSI variability properties is critical for understanding the cause of the irradiation variability from the Sun. A TSI data series has information that reflects the cause of the TSI variability. If the TSI variability has deterministic oscillating periods, we can
10 forecast expected TSI variation, whereas a random TSI variability can only explain the past. The intermittency of the solar variation is preferably explained as stochastic noise (Charbonneau, 2010). In this investigation, we introduce a simple hypothesis: if the TSI variability has a periodic oscillation, the variability oscillation must have an oscillation source that influences the solar energy
15 oscillation. A possible oscillation source is the oscillating gravity between the Sun and the large planets.

1.1. Solar variability

The concept of a perfect and constant Sun, as postulated by Aristotle, was undisputed for many centuries. Although some transient changes of the Sun
20 were observed with the naked eye, the introduction of the telescope in approximately 1600 demonstrated that the Sun had spots that varied in number and location. From 1610 systematic observations were reported. A pattern of sunspot variations was established when Heinrich Schwabe began regular observations of sunspots in 1826. He reported a possible period of approximately ten years
25 (Schwabe, 1844). Wolf (1859) presented the opinion that the planets Venus, Earth, Jupiter and Saturn modulate the solar variability.

The solar activity cycle (Hathaway, 2015) consists of dark sunspots and bright regions (faculae) in addition to active regions that display sudden energy releases (flares). The average cycle length is 11.1 years. During a cycle, the
30 number of spots increases to a maximum number and then decreases. The average lifetime of a sunspot is slightly longer than the solar rotation period. They are bipolar, with the same magnetic polarity that leads with respect to the direction of the solar rotation. When the next cycle starts, spots appear with opposite polarity at high latitudes in both hemispheres, and as the cycle
35 progress, they appear closer to the Equator.

The 11.1-year sunspot period is referred to as the Schwabe cycle, and is proposed to be created by the tidal torque from the planets Venus, Earth and Jupiter (Wilson, 2013). The 22-year magnetic reversal period is referred to as the Hale period. Scafetta (2012) showed that the 11-year Schwabe sunspot cycle
40 consists of three periods of 9.98, 10.90 and 11.86 years, which are close to the Jupiter/Saturn spring period of 9.93 years, a tidal pattern of Venus, Earth and Jupiter of 11.07 years and the Jupiter orbital period of 11.86 years. A relation between the planets periods and sunspot periods indicates the possibility of a deterministic long-term relation between planet periods and hidden periods in
45 sunspot data series.

1.1.1. Sunspot data series

The sunspot number time series is a measure of the long-term evolution of the solar cycle and the long-term influence of the Sun on the Earth's climate. The relative sunspot number (R) as defined by Wolf (1861) is based on the total
50 number of individual sunspots n and the number of sunspot groups g , according to the formula $R = k(10g + n)$, where k is a correction factor for the observer. It was introduced to correct for the use of different telescopes and observers. R is referred to as the Zürich, Wolf or International Sunspot Number. Today SN is used for the International Sunspot Number (Clette et al., 2014).

55 Rudolf Wolf started systematic observations of sunspot numbers in 1849. He also collected previous observations to construct daily sunspot numbers to 1750 and a yearly series to 1700. The cycle that started in 1755 became sunspot cycle 1. The sunspot numbers had to be scaled upwards several times due to missing spots. By approximately doubling the number of recovered observations
60 and cleverly interpolating between sparse observations (Hoyt et al., 1994), gaps were reduced and the series was extended to the first recording of sunspots by telescope in 1611. The history of the sunspot series and the last extensive corrections are described by Clette et al. (2014). The revised yearly series, which is available from the World Data Center SILSO from July 2015, was employed
65 in our analysis.

Because the standard sunspot series is a composite time series based on single spots and groups, the accuracy significantly decreases the possibility of going back in time. Similar to poorer telescopes and locations, smaller spots were difficult to see and frequently lost. To correct for this situation, Hoyt and Schatten
70 (1998a,b) constructed a new group sunspot number R_G that was normalized to the Zürich sunspot number. Their series covered the period 1610-1995 and was based on a larger and more refined observational database. Although the group sunspot number corresponded to the relative sunspot number in the 20th century, the maximum group number was 40% lower in the 19th century and
75 previous centuries (Clette et al., 2014). The group sunspot numbers were recently revised, and the difference between the series may now be considered as random noise. However, during the last two sunspot cycles (nos. 23 and 24), 30% fewer sunspots per group were observed, which may be a sign of changes in the solar dynamo (Clette et al., 2014).

80 1.1.2. *Solar activity periods – grand maxima and minima*

In the 1890s, G. Spörer and E. W. Maunder (Maunder, 1890) reported that the solar activity was strongly reduced over a period of 70 years from 1645 to 1715 (Eddy, 1976, 1983). Based on naked-eye observations of sunspots, records of aurora activity, and a relation between ^{14}C variations and solar activity, a
85 grand maximum (1100-1250) and the Spörer minimum (1460-1550) were also identified (Eddy, 1976).

The distribution of the solar activity can be interpreted as bi-modal, which implies distinct modes of activity. The main (regular) mode corresponds to moderate activity, which has a maxima of the 10-yr average spot number be-
90 tween 20 spots and 67 spots. In addition, we obtain grand maxima and grand minima that are above this range and below this range, respectively (Usoskin et al., 2014). Studies that employ cosmogenic isotope data and sunspot data indicate that we are currently leaving a grand activity maximum, which started in approximately 1940 and is now declining (Usoskin et al., 2003; Solanki et al.,
95 2004; Abreu et al., 2008).

Because grand maxima and minima occur on centennial or millennial timescales, they can only be investigated using proxy data, i.e., solar activity reconstructed from ^{10}Be and ^{14}C time-calibrated data. The conclusion is that the activity level of the Modern Maximum (1940-2000) is a relatively rare event, with the
100 previous similarly high levels of solar activity observed 4 and 8 millennia ago (Usoskin et al., 2003). Nineteen grand maxima have been identified by Usoskin et al. (2007) in an 11,000-yr series.

Grand minimum modes with reduced activity cannot be explained by only random fluctuations of the regular mode (Usoskin et al., 2014). They can be
105 characterized as two flavors: short minima in the length range of 50-80 years (Maunder-type) and longer minima (Spörer-type). Twenty-seven grand minima are identified with a total duration of 1900 years, or approximately 17% of the time during the last 11,500 years (Usoskin et al., 2007). An adjustment-free reconstruction of the solar activity over the last three millennia confirms four
110 grand minima since the year 1000: Maunder (1640-1720), Spörer (1390-1550), Wolf (1270-1340) and Oort (1010-1070) (Usoskin et al., 2007). The Dalton minimum (1790-1820) does not fit the definition of a grand minimum; it is more likely a regular deep minimum that is observed once per century or an immediate state between the grand minimum and normal activity (Usoskin et al., 2013).

115 Temperature reconstructions for the last millennium for the northern hemisphere (Ljungquist, 2010) show a medieval maximum temperature at approximately the year 1000 and a cooling period starting at approximately 1350, immediately after the Wolf minimum and lasting nearly 500 years, with the coldest period in what is referred to as the Little Ice Age (LIA) at the time of
120 the Maunder minimum. A cold period was also observed during the time of the Dalton minimum. The Maunder and the Dalton minima are associated with less solar activity and colder climate periods. In this investigation, minimum solar activity periods may serve as a reference for the identified minimum irradiances in the TSI oscillations.

125 *1.2. Total Solar Irradiance*

The total solar irradiance (TSI) represents a direct index for the luminosity of the Sun measured at the Earth's average distance from the Sun. The solar luminosity was previously considered to be constant, and the TSI was also named the solar constant. Since satellite observations started in 1979, the total solar intensity (TSI) has increased by approximately 0.1% from the solar minima to the solar maxima in the three observed sunspot periods. The variation in the TSI level does not adequately explain the observed variations in the global temperature. In addition to the direct effect, however, many indirect effects exist, such as UV energy changes that affect the production of ozone, solar wind modulation of the galactic cosmic ray flux that may affect the formation of clouds, and local and regional effects on temperature, pressure, precipitation (monsoons) and ocean currents. The Pacific Decadal Oscillation (PDO) and the North Atlantic Oscillation also show variations that are related to the phase of the TSI (Velasco & Mendoza, 2008). A significant relation between sunspots and ENSO data has also been observed (Hassan et al., 2016).

Composite TSI records have been constructed from a database of seven independent measurement series that cover different periods since 1979. Different approaches to the selection of results and cross-calibration have produced composites with different characteristics: the Active Cavity Radiometer Irradiance Monitor (ACRIM) and the Physikalisch-Meteorologisches Observatorium Davos (PMOD) series. The ACRIM composite uses the TSI measurements that were published by the experimental teams (Willson, 2014), whereas the PMOD composite uses a proxy model that is based on the linear regression of sunspot blocking and faculae brightening against satellite TSI observations (Frölich & Lean, 1998). To construct a TSI from a previous time period, two different approaches are employed: a reconstruction that is based on several different proxies for the sun's irradiance (ACRIM) or a statistical approach (PMOD). Proxies for the Sun's irradiance include the equatorial solar rotation rate, the sunspot structure, the decay rate of individual sunspots, the number of sunspots without umbra, the length and decay rate of the sunspot cycle, and the solar activity

level.

Hoyt & Schatten (1993) constructed an irradiance model that was based on the solar cycle length, cycle decay rate, and mean level of solar activity for the period 1700-1874. From 1875-1992, a maximum of five solar indices were employed. The correlation between these indices and the phase coherence indicated that they have the same origin. Hoyt & Schatten (1993) interpret this finding as a response to convection changes near the top of the convection zone in the Sun. All solar indices have maxima between 1920 and 1940; the majority of the maxima occur in the 1930s. The Hoyt-Schatten irradiance model has been calibrated and extended with the newest version of ACRIM TSI observations (e.g. Scafetta & Willson, 2014, Fig. 16); it is employed in this analysis. In the following section, this reconstruction is referred to as TSI-HS. A mostly rural Northern Hemisphere composite temperature series 1880 -2013 show strong correlation with the TSI-HS reconstruction, which indicates a strong solar influence on Northern Hemisphere temperature (Soon et al., 2015).

The TSI-HS series covers the period from 1700-2013. To investigate longer periods to search for minimum periods, we have employed a statistical TSI index that was estimated by Velasco Hererra et al. (2015) from 1000 to 2100. The index, which is referred to as TSI-LS, is estimated by the least squares support vector machine (LS-SVM) method, which is applied for the first time for this purpose. The method is nonlinear and nonparametric. The starting point is a probability density function (PDF) that was constructed from the PMOD and ACRIM composites. The function describes how many times a certain level of TSI has been observed. From this normalized annual power, anomalies are constructed. The TSI between 1610 and 1978 was determined by the LS-SVM method using the group sunspot number as an input after calibration between 1979 and 2013 with the ACRIM or PMOD composites. To estimate the TSI from 1000 to 1510 and from 2013 to 2100, the LS-SVM method and a nonlinear autoregressive exogenous model (NARX) were employed. In this study, we have employed the TSI reconstruction that was calibrated by the ACRIM TSI composite (Velasco Hererra et al., 2015).

1.3. Solar energy oscillation

An oscillation TSI variability is produced by irradiation from an oscillating energy source. This oscillation energy source may be the solar inertial motion, processes in the interior of the Sun, solar tide and/or solar orbit oscillation around the solar system barycenter (SSB). The energy source for the solar activity is the deceleration of the rotation of the Sun by magnetic field lines that are connected to interplanetary space. The solar wind carries mass away from the Sun; this magnetic braking causes a spin down of the solar rotation. Part of the decrease in rotational energy is the energy source for the solar dynamo, which converts kinetic energy to electromagnetic energy.

The classical interpretation of the solar dynamo is that it is placed in the transition zone between convection and radiation near the solar surface: the tachocline, approximately 200,000 km below the surface. Strong electric currents originate by the interaction between the convection and the differential solar rotation, which causes the formation of strong magnetic fields, which rise to the surface and display various aspects of solar activity, such as spots, facular fields, flares, coronal mass emissions, coronal holes, polar bright points, and polar faculae, after having detached, as described by De Jager & Duhau (2011). They explain the 22-year Hale cycle as attributed to magneto-hydrodynamic oscillations of the tachocline. This period is not constant and persisted for approximately 23 years prior to the Maunder Minimum, during which it increased to 26 years. During the maximum of the last century, this period was as brief as 21 years. Gleissberg (1958, 1965) discovered a cycle of approximately 80 years in the amplitude of the sunspot numbers. It is interpreted as the average of two frequency bandsone band from 50-80 years and one band from 90-140 years (Ogurtsov et al., 2002). An examination of the longest detailed cosmogenic isotope record (INTCAL98) of ^{14}C abundance, with a length of 12,000 years, reveals an average Gleissberg cycle period of 87.8 years. It is resolved in two combination periods of 91.5 ± 0.1 and 84.6 ± 0.1 yr (Peristykh & Damon, 2003).

Proxies that describe the magnetic fields in the equatorial and polar regions can describe the variability of the tachocline. A proxy for the equatorial (or

toroidal) magnetic field is R_{max} (the maximum number of sunspots in two successive Schwabe cycles), and a proxy for the maximum poloidal magnetic field strength is aa_{min} (the minimum value of the measured terrestrial magnetic field difference). In a phase diagram based on the R_{max} and aa_{min} values, two Gleissberg cycles (1630-1724) and (1787-1880) are shown (Duhau & De Jager, 2008). The years 1630 and 1787 represent transition points, where phase transitions to the grand episodes (Maunder and Dalton minima) occurred. The lengths of the two Gleissberg cycles were 157 years and 93 years. The next Gleissberg cycle lasted 129 years until 2009 with an expected phase transition to a high state in 1924. Duhau & De Jager (2008) predicted that the transition in 2009 indicates a transition to a Maunder-type minimum that will start with cycle 25 in approximately 2020.

In addition to the variable Gleissberg period, a de Vries period from 170-260 years is observed in the ^{14}C and ^{38}Cl records. This period is fairly sharp with little or no variability (Ogurtsov et al., 2002). Almost no existing models for the solar activity predicted the current weak cycle 24. A principal component analysis of full disc magnetograms during solar cycles 21-23 revealed two magnetic waves that travel from opposite hemispheres with similar frequencies and increasing phase shifts (Shepherd et al., 2014; Zharkova et al., 2015). To understand this phase shift they introduce a non-linear dynamo model in a two-layer medium with opposite meridional circulation. One dynamo is located in the surface layer and the other dipole deeply in the solar convection zone. The solar poloidal field is generated by these two dynamos in different cells with opposite meridional circulation. The observed poloidal-toroidal fields have similar periods of oscillation with opposite polarities that are in an anti-phase every 11 years, which explains the Schwabe period. The double-cell meridional circulation flow is also detected with helioseismology by HMI/SDO observations (Zhao et al., 2013). Extrapolations backward of these two components revealed two 350-year grand cycles that were superimposed on a 22-year cycle. The beat between the two waves shows a remarkable resemblance to the sunspot activity, including the Maunder and Dalton minima, and forecasts a deep minimum in

this century. The low frequency wave has a variable period length from 320 year
250 (in 18-20 centuries) to 400 year predicted for the next millennium.

Another model is based on the observation that the thermal relaxation time
in the convection zone is on the order of 10^5 years (Foukal et al., 2009), which
is too long to explain the rapid decay of the magnetic field during one solar
cycle. A simple and elegant solution is to place the dynamo in small bubbles
255 in the solar core, which change polarity every cycle due to interaction with
the interplanetary magnetic field (Granpierre, 2015). The liberated rotational
energy then forms buoyant hot bubbles that move toward the solar surface.
These bubbles are observed on the solar surface as precursors for large flares.
The largest flares have a high probability of appearing near the closest position
260 of one or more of the tide-producing planets Mars, Venus, Earth and Jupiter
(Hung, 2007; Mörner et al., 2015). The energy of the hot bubbles is boosted
by thermonuclear runaway processes in the bubbles, which appear at the solar
surface as hot areas with a frozen magnetic field. In this process, planetary
effects serve an important role (Granpierre, 1990, 1996; Wolf & O'Donovan,
265 2007; Scafetta, 2012).

1.4. External forcing generated by the planets

Although the various dynamo models can explain the variations to some
extent, few or no constraints on the periods exist. The majority of the expla-
nations operate with a range of possible periods. The models do not explicitly
270 determine whether the observed periods are random and stochastic or if some
period-forcing from external or internal sources occurs. In the following section,
we investigate the external forcing that is generated by the planets in the solar
system.

1.4.1. Solar inertial motion

275 Charvátová & Heida (2014) have classified the solar inertial motion (SIM)
in an ordered (trefoil) pattern with a length of approximately 50 years and dis-
ordered intervals. Exceptionally long (approximately 370 years) trefoil patterns

appear with a 2402-year period (Hallstadt period). They determined that the deepest and longest solar activity minima (of Spörer and Maunder types) appeared in the second half of the 2402-year cycle, in accordance with the most disordered type of SIM. The Dalton minimum appeared during a mildly disordered SIM (1787–1843), which repeats from 1985-2040. The solar orbit in the period 1940-2040, which is shown in Figure 1, demonstrates this phase.

1.4.2. Interior of the Sun as a rotating star

Wolf & Patrone (2010) have investigated how the interior of a rotating star can be perturbed when the star is accelerated by orbiting objects, as in the solar system. They present a simple model in which fluid elements of equal mass exchange positions. This exchange releases potential energy (PE) that is only available in the hemisphere that faces the barycenter of the planetary system, with a minor exception. This effect can raise the PE for a few well-positioned elements in the Sun's envelope by a factor of 7, which indicates that a star with planets will burn nuclear fuel more effectively and have a shorter lifetime than identical stars without planets. However, occasional mass exchanges occur near the solar center, which activate a mixed shell situated at $0.16r_s$ where r_s is the solar radius. For this reason, the close passages of the barycenter are important because they can cause negative pulses in the PE. The energy is a result of the roto-translational dynamics of the cell around the solar system barycenter. An analysis of the variation of the PE storage reveals that the maximum variations correspond to the documented grand minima of the last 1000 years because the PE minima are connected to periods in which the Sun moves close to the barycenter. Large reductions in the PE values occur when the giant planets are quasi-aligned, which occurred in approximately 1632, 1811 and 1990, separated by 179 years (Jose cycle). Because the planetary positions never exactly repeat, the PE variations show a complex pattern that creates different minima (Cionco & Soon, 2015).

1.4.3. Solar inertial oscillations

The complex planetary synchronization structure of the solar system has been known since the time of Pythagoras of Samos (ca. 570-495 BC). Jose (1965) showed that the solar center moves in loops around the solar system barycenter (SSB). The average orbital period of 19.86 years corresponds to the heliocentric synodic period of Jupiter and Saturn. The modulation of the orbit by the outer planets Uranus and Neptune produces asymmetries in the orbital shape and period variations between 15.3 and 23.4 years (Fairbridge & Shirley, 1987). The solar motion differs from the Keplerian motion of planets and satellites in important ways. For instance, the velocity is some time highest when the distance from the Sun to the SSB is largest, and the solar angular momentum may vary by more than one order of magnitude over a period of ten years (Blizzard, 1981). An analysis of solar orbits from A.D. 816 – 2054 covered seven complete Jose cycles of 179 years and indicated that prolonged minima can be identified by two parameters: the first parameter is the difference in axial symmetry of the orbit, and the second parameter is the change in angular momentum (torque) about SSB. Based on these criteria, a new minimum should begin between 1990 and 2013 and end in 2091 (Fairbridge & Shirley, 1987).

The distance of the Sun from the barycenter, the velocity, and the angular momentum show the same periodic behavior. The motion of the solar center around the SSB is typically prograde; however, in 1811 and 1990, the Sun occasionally passes near the SSB in a retrograde motion. Because the 1811 event occurred at the time of the Dalton minimum, a new minimum may occur in approximately 1990 (Cionco & Soon, 2015).

Scafetta (2014) reviews the investigation of the patterns that are described by the Sun and planets. He concludes that modern research shows that the planetary orbits can be approximated by a simple system of resonant frequencies and that the solar system oscillates with a specific set of gravitational frequencies, many of which range between three and 100 years, that can be constructed as harmonics of a base period of ~ 178.78 years.

1.4.4. Solar tidal oscillation

The tidal elongation at the solar surface is on the order of 1-2 mm from the planets Venus and Jupiter with less tides from the other planets. Scafetta (2012) proposed that tidal forces, torques and jerk shocks act on and inside the Sun and that the continuous tidal massaging of the Sun should involve heating the core and periodically increasing the nuclear fusion rate. This action would amplify weak signals from the planets with a factor $\sim 4 \times 10^6$. Even if the amplitude is small in the direction of a planet, it creates a wave that propagates with the velocity of the planet. If the planet has an elliptical orbit, the variation in distance creates a disturbance that will affect the nuclear energy production in the center of the Sun. Since more planets participate, the effect will be a combination of phases and periods, which can be highly nonlinear.

Our hypothesis is that the solar position oscillation (SPO) represents an indicator of the tidal and inertial interaction between the giant planets Jupiter, Saturn, Neptune, Uranus and the Sun. The SPO can be calculated from planetary Ephemeris as the movement of the Sun around the Solar System Barycenter (SSB). In section 2, we describe the methods and data sets used to demonstrate a connection between SPO and TSI and SN variations. In section 3, we present the results; in section 4, we discuss the results and relate them to other investigations. We conclude the paper in section 5. Because the solar system and its planets has a long lifetime, we can expect forces in the same direction over long periods of time that may have a strong effect on long periods.

2. Materials and methods

2.1. Data

The motive of the study is to identify possible stationary periods in TSI variability. In this study possible stationary periods are represented by first stationary periods, subharmonic periods and coincidence periods. First stationary periods have a period T in the data series. Subharmonic periods have periods $n * T$ for $n = 2, 3, 4 \dots$. Coincidence periods have a coincidence between

365 two or more periods and may be represented by $n * T_1 = m * T_2$. Coincidence
 periods are stationary periods and introduce a new set of subharmonic periods.
 The study compares the identified stationary periods and period phase in two
 TSI data series, a sunspot data series and a SPO data series.

The SPO data series represents an indicator of the oscillating tidal and in-
 370 ternal interaction between the Sun and the large planets. The large planets
 have the following periods (in years): Jupiter $P(J, 11.862)$, Saturn $P(S, 29.447)$
 , Uranus $P(U, 84.02)$ and Neptune $P(N, 164.79)$. The SPO covers the pe-
 riod from 1000 to 2100, where SPO_x represents the x -direction of the xyz -
 vector. The source of the SPO data series is the JPL Horizon web interface
 375 (<http://ssd.jpl.nasa.gov/horizons.cgi#top>), which is based on the Re-
 vised July 31, 2013 ephemeris with the ICRF/J2000 reference frame, down-
 loaded 30.09.14 and at subsequent dates.

The total solar irradiance (TSI-HS) data series (e.g. Scafetta & Willson,
 2014, Fig. 16) covers the period from 1700 to 2013. The source of the data series
 380 is Scafetta (personal communication. Dec. 2013). The total solar irradiation
 (TSI-LS) is based on the LS-SVM ACRIM data series (Velasco Herrera et al.,
 2015) and covers the period from 1000 to 2100. The source of the TSI-LS data
 series is Velasco Herrera (21.09.14. Personal communication). The sunspot
 data series is the group sunspot numbers from 1610 to 2015. The source of
 385 the sunspot data series is SILSO (The World Data Center for the production,
 preservation and dissemination of the international sunspot number).

2.2. Methods

Possible stationary periods in the data series are identified in two steps. First
 a wavelet transform of the data series separates all periods in into a wavelet
 390 spectrum. The autocorrelation for wavelet spectrum then identifies dominant
 first stationary periods, subharmonic periods and the coincidence periods. Prior
 to the wavelet analysis, all data series are scaled by

$$x(t) = (y(t) - E[y(t)]) / \text{var}(y(t)) \quad (1)$$

where $y(t)$ is the data series, $E[y(t)]$ is the mean value, $var(y(t))$ is the variance and $x(t)$ is the scaled data series. The data series are scaled to compare
 395 the amplitudes from the oscillation periods and reduce side effects in the wavelet analysis.

A wavelet transform of a data series $x(t)$ has the ability to separate periods in the data series into a wavelet spectrum. The wavelet spectrum is computed by the transformation

$$W_{a,b(t)} = \frac{1}{\sqrt{a}} \int_R x(t) \psi\left(\frac{t-b}{a}\right) dt \quad (2)$$

400 where $x(t)$ is the analyzed time series, $\psi()$ is a `coif3` wavelet impulse function (Daubechies, 1992; Matlab, 2015); which is chosen for its symmetrical performance and its ability to identify symmetrical periods in data series; $W(a, b(t))$ represents the computed wavelet spectrum, the parameter a represents a time-scaling parameter, and the parameter b represents a translation in time in the
 405 wavelet transformation. When translating $b = 0$ and $s = 1/a$, the wavelet spectrum $W(s, t)$ represents a set of moving correlations between $x(t)$ and the impulse function $\psi()$ over the entire time series $x(t)$. The relationship between the wavelet s and a sinus period T is approximately $T \sim 1.2s$ when using the `coif3` wavelet function. In this investigation, the wavelet spectrum $W(s, t)$ has
 410 the spectrum range $s = 0, 1, 2 \dots 0.6N$, where N is the number of samples in the data series.

An autocorrelation transformation of the wavelet spectrum $W(s, t)$ identifies first periods, subharmonic periods and coincidence periods as maximum values in the computed set of autocorrelation functions. The set of autocorrelation
 415 functions are estimated by the transformation

$$R(s, m) = E[W(s, t)W(s, t + m)] \quad (3)$$

where $R(s, m)$ represents the correlations between samples, at a distance m years, for a wavelet s in the wavelet spectrum $W(s, t)$.

3. Results

3.1. Sun Position Oscillation

420 The Sun moves in a closed orbit around the barycenter of the solar system. Figure 1 shows the SPO in the ecliptical plane from 1940 to 2040. The solar system oscillation (SSO) is caused by the mutual gravity dynamics between the planet system oscillation (PSO) and the solar position oscillation (SPO). The solar position oscillation has oscillations in the (x, y, z) directions; they are
425 represented by the data series $SPOx$, $SPOy$ and $SPOz$. The movement looks rather chaotic, as shown in Figure 1, because it mirrors the movements of the planets in their orbits. A first step in this investigation is to identify stationary periods and phase relations in the solar position between year 1000 and year 2100.

430 A wavelet spectrum represents a set of moving correlations between a data series and a scalable wavelet pulse. When the data series in the y-direction - $SPOy$ - is transformed to the wavelet spectrum $Wspoy(s, t)$, the spectrum represents a collection of dominant periods in the $SPOy$ data series. A visual inspection of the wavelet spectrum $Wspoy(s, t)$ shows a long-term dominant
435 period of approximately $Pspoy(164)$ years. This period has a coincidence to the Neptune period $P(N, 164.79)$. The data series $SPOx$ and $SPOy$ have the same periods; however, $SPOy$ has a 90-degree phase delay.

The wavelet spectrum $Wspoy(s, t)$ is transformed to a set of autocorrelation functions $Rspoy(s, m)$, as shown on Figure 2, where each colored function represents a single autocorrelation. The set of autocorrelations $Rspoy(s, t)$ shows
440 the identified stationary periods in the wavelet spectrum $Wspoy(s, t)$. The first maximum represents the correlation to a first stationary period. Subharmonic periods have a maximum correlation at a distance first period $\times n$ where $n = 1, 2, 3, \dots$. $Rspoy(s, m)$ identifies stationary periods $P(spoym, 12)$ for $Rspoy(12) =$
445 $0.98, P(spoym, 29)$ for $Rspoy(29) = 0.95, P(spoym, 84)$ for $Rspoy(84) = 0.9$ and $P(spoym, 164)$ for $Rspoy(164) = 0.9$. The same periods are associated with the PSO periods $P(J, 11.862), P(S, 29.447), P(U, 84.02)$ and $P(N, 164.79)$, which in-

dicates that the planets Jupiter, Saturn, Uranus and Neptune in the planetary system are controlling the SPO.

450 A coincidence between subharmonic periods will amplify the coincidence period and introduce a new set of stationary periods. The autocorrelation spectrum $Rspoy(s, m)$ of Figure 2 shows a set of subharmonic periods - $P(spoyn, n * 12)$, $P(spoyn, n * 29)$ and $P(spoyn, n * 84)$ - where $n = 1, 2, 3, \dots$. The identified coincidence periods have mean values of

455 $(P(spoyn, 5 * 12) + P(spoyn, 2 * 29))/2 = P(spoyn, 59)$ for $RW(spoyn, 59) = 0.95$,
 $P(spoyn, 7 * 12) + P(spoyn, 3 * 29) + P(spoyn, 84))/3 = P(spoyn, 85)$ for $RW(spoyn, 85) = 0.9$,

$(P(spoyn, 10 * 12) + P(spoyn, 4 * 29))/2 = P(spoyn, 118)$ for $Rspoy(118) = 0.9$
and $(P(spoyn, 2 * 84) + P(spoyn, 164))/2 = P(spoyn, 166)$ for $Rspoy(166) = 0.9$.

460 Figure 2 reveals that the majority of the SPO periods are mutually related by resonance. The new modulated periods are $P(spoyn, 59)$ and $P(spoyn, 118)$.

The stationary long wavelet periods $Wspoy(84, t)$ and $Wspoy(164, t)$ have maxima in approximately 1820, and $Wspoy(29, t)$ has a maximum in approximately 1812. The identified stationary periods may be transformed to the
465 model:

$$P(spoyn, 29, t) = RW(spoyn, 29) \cos(2\pi(t - 1812))/29.447 \quad (4)$$

$$P(spoyn, 84, t) = RW(spoyn, 85) \cos(2\pi(t - 1820))/84.02 \quad (5)$$

$$P(spoyn, 164, t) = RW(spoyn, 164) \cos(2\pi(t - 1820))/164.97 \quad (6)$$

By this model, the year 1820 may serve as a phase reference for the $SPOy$ periods, TSI variability and solar variability (SN). The data series $SPOx$ in has the same stationary periods but a different phase. $P(spoyn, 84, t)$ has a maximum at approximately 1797, which represents a phase shift of approximately
470 $\pi/2$. $P(spoyn, 164, t)$ has a maximum at approximately 1779. The maxima in $SPOy$ and $SPOx$ corresponds to minima in $SPOj$ and $SPOx$. The deterministic model has the sum $P(spoyn, 29, t) + P(spoyn, 84, t) + P(spoyn, 164, t)$ and a maximum in approximately 1812.

3.2. TSI-HS variability

475 The total solar irradiation (TSI) represents the measured irradiation Wm^{-2}
from the Sun to the Earth. Figure 3 shows an annual mean total solar irradiance
(TSI-HS) data series (Scafetta & Willson, 2014) that covers the period from 1700
to 2013. A simple visual inspection of this data series shows some variability
properties. The TSI-HS data series irradiation has fluctuations of approximately
480 $3\text{-}4 \text{ Wm}^{-2}$. The TSI fluctuations have minima in approximately 1700 (or
before), 1800, 1890, and 1960, with gaps of approximately 100, 90, and 70
years, or a mean minimum period of approximately 86 years. The TSI-HS data
series has maxima in 1770, 1830, and 1950, with gaps of approximately 60 and
120 years. The mean maximum fluctuation period in the TSI-HS data series
485 is approximately 75 years or 11 years less than the mean minimum period.
Transformation of the TSI data series into a wavelet spectrum may identify
stationary periods.

The transformed wavelet spectrum $Whs(s, t)$ represents a set of separated
wavelet periods from the TSI-HS data series. Figure 4 shows the computed
490 wavelet spectrum of the TSI-HS data series from 1700 to 2013. In this presen-
tation, the wavelet scaling range is $s = 1 \dots 0.6N$, and the data series contains
 $N = 313$ data points. A visual inspection of the TSI wavelet spectrum shows
the dominant periods in the TSI data series in the time window between 1700
and 2013. The long wavelet period has a maximum in 1760, 1840, 1930, and
495 2000, with a mean gap of approximately 80 years.

The autocorrelation spectrum $Rhs(s, m)$ of the wavelet spectrum $Whs(s, t)$
identifies hidden stationary periods in the wavelet spectrum. The maximum
values in the autocorrelation spectrum $Rhs(s, m)$ represent a correlation to sta-
tionary periods in the TSI-HS wavelet spectrum. Figure 5 shows the autocor-
relation spectrum $Rhs(s, m)$ of the wavelet spectrum $Whs(s, t)$ of the TSI-HS
500 data series.

A study of the autocorrelation spectrum $Rhs(s, m)$ shows a set of stationary
periods in the $Whs(s, t)$ wavelet spectrum. The identified first cause station-
ary periods comprise the period set $P(hs, 11)$ for $Rhs(11) = 0.55$, $P(hs, 49)$ for

505 $Rhs(49) = 0.55, P(hs, 86)$ for $Rhs(86) = 0.65$ and $P(hs, 164)$ for $RWhs(164) =$
 0.7. The identified stationary periods are associated with the PSO periods
 $P(J, 11.862), P(S, 29.447), P(U, 84.02)$ and $P(N, 164.79)$. The identified sta-
 tionary period $P(hs, 49)$ is explained by a modulation between the Saturn os-
 cillation and the Neptune oscillation: $2/(1/P(S, 29.447) + 1/P(N, 164.79)) =$
 510 $P(S, N, 49.96)$. This finding indicates that the TSI-HS variability is related
 to the solar position oscillation, which is controlled by the planet oscillation
 from the large planets Jupiter, Saturn, Uranus and Neptune. Additional analy-
 sis indicates that the dominant wavelet periods $Whs(11, t)$ and $Whs(49, t)$ are
 mean estimates. $Whs(11, t)$ has phase disturbance and $Whs(49, t)$ has a phase-
 515 reversal, as shown in Figure 6. They do not have a stable phase and represent
 mean periods.

Figure 6 shows the identified dominant stationary wavelet periods $Whs(49, t)$,
 $Whs(86, t)$ and $Whs(165, t)$ from the autocorrelation functions in $Rhs(s, m)$. It
 shows that the wavelet period $P(hs, 49)$ has a time-variant phase and is not a
 520 stable period. The TSI-HS wavelet periods $Whs(49, t)$ and $Whs(86, t)$ have a
 negative value coincidence in the period from 1786 to 1820. $Wspoy(84, t)$ has an
 estimated maximum velocity and $Wspox(84, t)$ has maximum state at approx-
 imately 1797. The dominant wavelet period $Whs(84, t)$ has a minimum state
 at approximately 1803, or a phase delay of approximately 0.15π between the
 525 $Wspox(84, t)$ maximum and the minimum $Whs(84, t)$. Uranus was in perihelion
 in 1798. This indicates a relation between a minimum Uranus distance to the
 Sun and a minimum in TSI-HS.

The correlation between the TSI-HS data series and the identified domi-
 nant wavelet periods $Whs(49, t) + Whs(86, t) + Whs(164, t)$ is estimated to be
 530 $R = 0.93, Q = 46.6$ (Pearson correlation coefficient) in $N = 312$ samples. The
 correlation $R = 0.93$ reveals a close relation between the TSI-HS variability and
 the solar position oscillation, which is controlled by Jupiter, Saturn, Uranus and
 Neptune.

3.2.1. Deterministic model

535 The identified stationary periods $Whs(86, t)$ and $Whs(164, t)$ may be represented by a deterministic model from the sum of the stationary cosine functions:

$$P(hsc, 84, t) = -Rhs(86) \cos(2\pi(t - 1803)/84.02) \quad (7)$$

$$P(hsc, 164, t) = -Rhs(164) \cos(2\pi(t - 1860)/164.97) \quad (8)$$

$$P(hsc, t) = P(hsc, 84, t) + P(hsc, 164, t) \quad (9)$$

where $R(hs, 86)$ and $R(hs, 164)$ represent estimated correlations in the autocorrelation. The phase relation between the maximum value of $Pspox(84, t)$ in 1797 and the minimum value $P(hsc, 84, t)$ in 1803 is approximately 0.15π (rad/year).
 540 The year 1797 is also the year of Uranus in perigel. We also notice that the minimum value of $P(hs, 164, t)$ (Eq. 8) is close to the time of Neptune in perihel. This indicates a delayed response from the SPO periods on the TSI-HS variability. The correlation between the 84-year wavelet periods $P(hsc, 84, t)$ and $W(hsc, 84, t)$ is estimated to be $Rhs, hsc(84) = 0.83$. The correlation between
 545 the 164-year periods is $Rhs, hsc(164) = 0.88$. The correlation between the data series TSI-HS and the sum $P(hsc, t)$ is estimated to be $R = 0.55$. These results indicate that the dominant wavelet periods $Whs(84, t)$ and $Whs(164, t)$ have stable phases from 1700 to 2013.

From the deterministic model (Eq. 9) of the data series TSI-HS, we estimate
 550 grand minimum periods when $P(hsc, t) \leq -1$. These minima, which are compared with named solar minima, are shown in Table 2. The next deep minimum is estimated at approximately 2050. The TSH-HS data series can estimate time period up to a maximum of $(2013-1700)/2=156$ years and supports reasonable good estimates of periods of approximately one hundred years. Longer time
 555 period estimates require longer data series.

3.3. TSI-LS variability

The TSI-LS data series (Figure 7) covers a period of 1100 years from 1000 to 2100, where the time period from the present to 2100 is forecasted. A realistic

hundred-year forecast or hindcast has to be based on possible hidden determin-
560 istic periods in the data series. A coherence analysis of the wavelet spectra
 $Whs(s, t)$ and $Wls(s, t)$ shows a coherency $Chs, ls = 0.8 - 0.95$ for periods be-
between 48 years and 86 years, which indicates that the TSI-HS data series and
the TSI-LS data series have the same periods from 48 - 86 years from 1700 to
2013.

565 The data series TSI-LS is analyzed by computing the wavelet spectrum
 $Wls(s, t)$ and the autocorrelation spectrum $Rls(s, m)$, the latter shown in Figure
8. The identified stationary periods in the autocorrelation spectrum $Rls(s, m)$
are $P(ls, 11)$ for $Rls(11) = 0.8$, $P(ls, 18)$ for $Rls(18) = 0.3$, $P(ls, 29)$ for
 $Rls(29) = 0.2$, $P(ls, 83)$ for $Rls(83) = 0.17$, $P(ls, 125)$ for $Rls(125) = 0.6$,
570 $P(ls, 210)$ for $Rls(210) = 0.35$ and $P(ls, 373)$ for $Rls(373) = 0.5$, the last not
shown in Fig. 8. These periods are associated with the identified stationary
periods in the TSI-HS data series, the SPO data series periods and the PSO pe-
riods $P(J, 11.862)$, $P(S, 29.447)$ and $P(U, 84.02)$. The difference is the smaller
correlation value in the autocorrelation $Rls(s, m)$. Smaller correlation values
575 may be explained by phase errors in this long data series.

The autocorrelation spectrum $Rls(s, m)$ (Figure 8) shows coincidence peri-
ods between $P(ls, 3 * 11) = P(ls, 33)$ and $P(ls, 2 * 18) = P(ls, 36)$, between
 $P(ls, 5 * 11) = P(ls, 55)$ and $P(ls, 3 * 18) = P(ls, 54)$, and between $P(ls, 8 * 11) =$
 $P(ls, 88)$ and the first period $P(ls, 83)$. The coincidence period $P(ls, 55)$ in-
580 troduces the subharmonic periods $P(ls, n * 55)$ for $n = 1, 2, 3, \dots$. The new
information in $Rls(s, m)$ is an identification of the dominant first cause pe-
riods $P(ls, 18)$, $P(ls, 125)$ and $P(ls, 210)$. These periods have a combination
resonance that is created by a $2/3$ resonance and a $5/2$ resonance. The sta-
tionary model has a perfect relation to the Jupiter period and the Uranus
585 period when $P(ls, 18) = P(ls, 3 * 11/2)$ is related to $P(ls, 3 * 11.862/2 =$
 $17.793)$, $P(ls, 126) = P(ls, 3 * 84/2)$ is related to $P(ls, 3 * 84.02/2 = 126.03)$ and
 $P(ls, 210) = P(ls, 5 * 84/2)$ is related to the period $P(ls, 5 * 84.02/2 = 210.05)$.
The period $P(ls, 125)$ introduces a set of subharmonic periods $P(ls, n * 125)$,
where $n = 1, 2, 3, \dots$. In this investigation, we have only selected the third sub-

590 harmonic period $P(ls, 3 * 126.03 = 378.09)$, which is the most dominant.

The autocorrelation spectrum $Rls(s, m)$ shows that the period $Wls(125, t)$ represents the dominant amplitude variability in the TSI-LS data series. Figure 9 shows the identified long-term stationary periods $Wls(124, t)$, $Wls(210, t)$, $Wls(373, t)$ and the mean of the periods. The correlation between TSI-LS and the mean is estimated to be $R = 0.7$ for $N=1100$ samples and the quality $Q=27.4$. The mean of the identified wavelets $Wls(125, t)$, $Wls(210, t)$, $Wls(373, t)$ has a negative state in the periods (1000-1100), (1275-1314), (1383-1527), (1634-1729), (1802-1846) and (2002-2083). The mean has a minimum state in the years 1050, 1293, 1428, 1679, 1820, and 2040.

600 3.3.1. Deterministic model

The identified dominant periods $Wls(125, t)$, $Wls(210, t)$, and $Wls(373, t)$ may be represented by the deterministic stationary model from the sum of the cosine functions

$$P(lsc, 126, t) = Rls(125) \cos(2\pi(t - 1857)/(3 * 84.02/2)) \quad (10)$$

$$P(lsc, 210, t) = Rls(210) \cos(2\pi(t - 1769)/(5 * 84.02/2)) \quad (11)$$

$$P(lsc, 378, t) = Rls(373) \cos(2\pi(t - 1580)/(9 * 84.02/2)) \quad (12)$$

$$P(lsc, t) = P(lsc, 126, t) + P(lsc, 210, t) + P(lsc, 378, t) \quad (13)$$

where $Rls(125)$, $Rls(210)$ and $RWls(373)$ represent the maximum period correlations in the autocorrelation $Rls(s, m)$. The correlation between the 125-year wavelet period $Wls(125, t)$ and the stationary period $P(lsc, 126, t)$ is estimated to be $Rls, lsc(125) = 0.9$ for $N=1040$ samples and $Q=53.7$, $Rls, lsc(210) = 0.67$ for $N=1000$ and $Q=28.9$, and $Rls, lsc(378) = 0.68$ for $N=1000$ and $Q=28.8$. The period $P(lsc, 375, t)$ has the correlation $Rls, lsc(378) = 0.67$ to the identified wavelet period $Wls(373, t)$ for $N=1000$ samples and $Q=2813$. The dominant wavelet periods $Wls(125, t)$ and $Wls(375, t)$ have a stationary period and an approximately stable phase in the period from 1000 to 2100. A correlation of long data series is sensitive to phase noise. The sum of the stationary periods $P(lsc, t)$ represents a mean TSI-LS variability. The correlation to the TSI-LS

615 data series is estimated to be $Rlsc, ls(126 + 210 + 378) = 0.55$ for $N=1100$ and $Q=21.5$. This analysis indicates that the TSI-LS variability has been influenced by stationary periods that are controlled by the Uranus period $P(U, 84.02)$. A minimum of $P(lsc, 126, t)$ is in 1794, which is close to the time of Uranus perihel position, while $P(lsc, 2010, t)$ has a minimum in 1874 which is 0.7π after the
620 $Pspox(max)$. This indicates that the phase of these periods are synchronized with Uranus perihel position.

The deterministic model (Eq.11) of the data series TSI-LS may represent an index of minimum irradiation periods as shown in Table 2. By this index, the chosen data series references a TSI minimum when the state is $P(lsc, t) \leq -0.5$,
625 a Dalton-type minimum when $P(lsc, t) \leq -0.7$ and a grand minimum when $P(lsc, t) \leq -1.0$. The identified minima from this model are $P(lsc, t) \leq -1.0$ for the time period (1014-1056); $P(lsc, t) \leq -0.5$ for (1276-1301); $P(lsc, t) \leq -1.0$ for (1404-1435), which has a minimum -1.215 in the year 1419; $P(lsc, t) \leq -0.5$ for (1662-1695) which has a minimum -0.91 in the year 1672; and $P(lsc, t) \leq$
630 -0.5 for (1775-1819), which has a minimum -0.81 in the year 1796. The computed subsequent minimum time period is $P(lsc, t) \leq -0.5$ for (2035-2079), which has a minimum -0.79 in the year 2057. In this model, a Dalton-type minimum has a minimum at approximately -0.7. The Maunder minimum is between -0.7 and -1.0, as shown in Table 2. The computed minimum -0.79 in the year
635 2057 indicates an expected Dalton-Maunder-type minimum. The deterministic model state has a state $P(lsc, t) \geq +0.5$ index for the periods (1093-1134), (1198-1241) and (1351-1357); $P(lsc, t) \geq +1.0$ index for the period (1582-1610); $P(lsc, t) \geq +0.5$ for (1945-2013); and $P(lsc, t) \geq +1.0$ for (1959-2001), which has a maximum 1.4 in 1981.

640 3.4. Sunspot variability

The sunspot data series $SN(t)$ is an indicator of the solar variability. Figure 10 shows the group sunspot number data series that covers a period of approximately 400 years from 1610 to 2015. From this 400-year data series, we can estimate periods of approximately up to 200 years. Periods with few sunspots

645 are associated with low solar activity and cold climate periods. Periods with many sunspots are associated with high solar activity and warm climate periods. If a relation exists between solar periods and climate periods, we may expect a relation between the hidden periods in the TSI variability and solar variability.

Figure 11 shows the computed wavelet spectrum $Wsn(s, t)$ of the $SN(t)$ data series from 1610 to 2015, with the wavelet scaling parameter $s = 1 \dots 6N$. A visual inspection of the wavelet spectrum shows a maximum at the approximate years (1750, 1860, 1970), which represents periods of approximately 110 years. The time from 1750 to 1970 represents a period of 220 years. Temporary periods of approximately 50 years from approximately 1725 and 1930 may be confirmed by computing the autocorrelation wavelet spectrum $Rsn(s, t)$.

The computed set of autocorrelations $Rsn(s, m)$ of the wavelet spectrum $Wsn(s, t)$ is shown in Figure 12. The wavelet spectrum $W(sn, t)$ has the stationary periods $P(sn, 11)$ for $Rsn(11) = 0.73$, $P(sn, 22)$ for $Rsn(22) = 0.35$ and $P(sn, 86)$ for $Rsn(86) = 0.35$. The identified period $P(sn, 11)$ represents the Schwabe cycle and corresponds to the TSI $P(tsi, 11)$, the SPO period $P(spox, 11)$ and the Jupiter period $P(J, 11.862)$.

The period $P(sn, 11)$ introduces the subharmonic period $P(sn, 5 * 11) = P(sn, 55)$ for $Rsn(55) = 0.43$, which introduces the subharmonic periods $P(sn, 110)$ for $Rsn(110) = 0.40$ and $P(sn, 210)$ for $Rsn(210) = 0.36$. The period $P(sn, 55)$ is a temporary stationary period from 1610 only when $P(sn, 110)$ has a positive state. An inspection of $P(sn, 55)$ shows that the period is stationary when $P(sn, 210)$ has a positive state from 1726-1831 and from 1935. The period $P(sn, 55)$ shifted to $P(sn, 2*55)$ when $P(sn, 220)$ has a negative state from 1831-1935. A possible explanation is an $5/2$ relation between the periods $P(U, 84.04)$ and $P(sn, 210)$ (Eq. 16).

Figure 12 shows that the period $P(sn, 55)$ has combination resonance periods with a $3/2$ relation $P(sn, 3 * 55/2 = 84)$ to the Uranus period $P(U, 84.02)$. The $3/2$ correlation to the $P(ls, 84)$ period and the Uranus period $P(U, 84.02)$ explains the synchronization between the SN variability and the TSI-LS variability. The dominant period $P(sn, 110)$ is a coincidence period in the subhar-

monic period $P(sn, 2 * 55 = 110)$, which has a combination resonance to the Neptune period by $P(sn, 2 * 164, 79/3 = 109, 86)$. The long stationary identified period $P(sn, 210)$ is related to a $5/2$ combination resonance to Uranus by $P(U, 5 * 84.02/2 = 210.05)$. The period $P(sn, 210)$ corresponds to the TSI-
680 LS period $P(ls, 210)$. The identified periods have a subharmonic resonance in the Jupiter period $P(J, 11.862)$. The correlation between the data series $SN(t)$ and the dominant wavelet periods $W(sn, 55, t) + W(sn, 110, t) + W(sn, 210, t)$ is estimated to be $R = 0.51$ for $N=404$ and $Q=11.8$.

3.4.1. Deterministic model

685 The identified temporary stationary periods $Wsn(55, t)$, $Wsn(110, t)$ and $Wls(210, t)$ may be represented by a deterministic model

$$P(snc, 56, t) = Rsn(55) \cos(2\pi(t - 1782)/(2 * 84.02/3)) \quad (14)$$

$$P(snc, 112, t) = Rsn(110) \cos(2\pi(t - 1751)/(4 * 84.02/3)) \quad (15)$$

$$P(snc, 210, t) = Rsn(210) \cos(2\pi(t - 1770)/(5 * 84.02/2)) \quad (16)$$

$$P(snc, t) = P(snc, 56, t) + P(snc, 112, t) + P(snc, 210, t) \quad (17)$$

where $Rsn(56)$, $Rsn(112)$ and $Rsn(210)$ represent the maximum correlation in the autocorrelation $Rsn(s, m)$. This model is, however, a simplified linear model. Figure 11 shows that the $Rsn(55)$ amplitude is controlled by the
690 $Rsn(110)$ amplitude, which indicates that the period $P(sn, 55)$ is temporarily stable. The correlation between the 55-year wavelet periods $W(sn, 55, t)$ and the stationary period $P(snc, 55, t)$ is estimated to be $Rsn, snc(55) = 0.66$ for $N=354$ samples and $Q=16.6$. The correlations are $Rsn, snc(110) = 0.9$ for $N=304$ and $Q=36$ and $Rsn, snc(210) = 0.9$ for $N=304$ and $Q=36$. The correlation between
695 the sum $W(sn, 55, t) + W(sn, 110, t) + W(sn, 210, t)$ and the deterministic model from (Eq. 17) is estimated to be $R = 0.84$ for $N=304$ and $Q=29.8$. Minimum states that correspond to negative values of the stationary model correspond to the observed minima, as shown in Table 2. The model indicates a future minimum in the period 2018 - 2055 with an extreme value in 2035.

700 This analysis indicates that the sunspot variations is controlled by the Uranus
period $P(U, 84.02)$, which introduces a $2/3$ resonance to the period $P(sn, 55, t)$
and a $5/2$ super-resonance to the $P(sn, 210)$ period. The TSI-LS data series and
the sunspots data series have stationary coincidence periods with $P(ls, 11)$ and
 $P(sn, 11)$, $P(ls, 125)$ and $P(sn, 110)$ and with $P(ls, 210)$ and $P(sn, 210)$. The
705 difference between the stationary periods $P(ls, 125)$ and $P(sn, 110)$ indicates a
limited direct relation between the data series.

3.5. Stationary dominant periods and minima

The relations between the identified dominant periods in SN(t), TSI-HS and
TSI-LS are shown in Table 1, where R is the autocorrelation of the wavelet
710 spectrum..

In Table 2 we compare values of the stationary models $P(hsc, t)$, $P(lsc, t)$
and $P(snc, t)$ at minima corresponding to the solar activity minima determined
by Usoskin et al. (2007). The grand minimum periods are calculated from the
stationary models in Equations 9, 13 and 17, and compared with S_{pox} and S_{poy}
715 maxima. The model $P(snc, t)$ computes a new Dalton sunspot minimum from
approximately 2025 to 2050; the model $P(hsc, t)$ computes a new Dalton TSI
minimum period (2035-2065), and the model $P(lsc, t)$ computes a new Dalton
TSI minimum period (2045-2070).

The SN model in Eq. 17 is a simplified linear model. It has a minimum
720 $P(snc, t) \leq -0.5$ in 1907-1931, which is not shown in the table. The HS-model
from Eq. 9 has grand minima in 1200-120 and 1876-1887, which are not shown
in the table. For this model the Dalton minimum is less deep. The LS-model
from Eq. 13 has the maximum index $P(lsc, t) \geq 0.5$ for the periods (1093-
1134), (1198-1241), (1351-1357), and (1945-2013) and the grand maximum index
725 $P(lsc, t) \geq +1.0$ for the periods (1582-1610) and (1959-2001).

4. Discussion

The study of the TSI variability is based on the TSI-HS data series from
1700-2013, the TSI-LS data series 1000-2100, sunspots data series 1610-2015

and a Solar Barycenter orbit data series from 1000-2100. The results are, how-
730 ever, limited by how well they represent the solar physics and how well the
methods are able to identify the periods in the data series. The investiga-
tion is based on a new method. The data series are transformed to a wavelet
spectrum to separate periods, and the wavelets are transformed into a set of
autocorrelations to identify the first periods, subharmonic periods and coinci-
735 dence periods. The identified stationary periods in the TSI and SN series are
supported by the close relations with the well-known solar position periods and
documented solar minimum periods. The solar orbit data will then provide a
stable and computable reference. We have used the Dalton minimum (1790-
1820) as a reference period, since our two TSI-series and the SN-series cover
740 this minimum. We notice that maxima in $SPOx$ and $SPOy$ corresponds to
minima in $SPO\ddot{x}$ and $SPO\ddot{y}$ which means maximum negative acceleration. We
use $P(spoxc, 84, max) = 1797$ as a time of reference. This is close to the tim of
Uranus in perihelion (1798) and Neptune in aphelion (1804), which indicates a
possible relation between the distance to these planets and the minimum.

745 4.1. TSI-HS variability

The hidden dominant periods in the TSI-HS variability are related to the
large planets, as shown in Table 1. The correlation between the TSI-HS data
series and the identified dominant wavelet periods $Whs(49, t) + Whs(86, t) +$
 $Whs(164, t)$ is estimated to be $R = 0.93$. The dominant periods $P(hs, 11)$ and
750 $P(hs, 49)$ have a time-variant phase and represent mean estimates. A possi-
ble source of the $P(hs, 49)$ period is the interference between the Saturn pe-
riod $P(hs, 29)$ and the Neptune period $P(hs, 164)$. The periods $P(hs, 84)$ and
 $P(hs, 164)$ have a stable period and phase in the time period from 1700 to
2013. The TSI-HS data series from 1700 is too short for a reasonable estimate
755 of $P(hs, 164)$. A possible alternative is a coincidence resonance between the
subharmonic period $P(hs, 2 * 84 = 168)$ and the 164 year Neptune period.

The model $P(hsc, t)$ computes the deterministic oscillations in the TSI-HS
variability. Table 2 shows that $P(hsc, t)$ computes a minimum in the period

from 1796-1830. In the same time period, $P(sprox, 84)$ and $P(spoym, 84)$ have
760 maxima in 1797 and 1820. A close relation between the minimum of the period
 $P(hs, 84)$ and the maximum states of $P(sprox, 84)$ and $P(spoym, 84)$ is observed.

The identified wavelet stationary periods $Whs(84, t)$ and $Whs(164, t)$ are
transformed to a simplified model in Eq. 9, which produces a simplified deter-
ministic TSI-HS data series from 1000 to 2100. The computed results in Table
765 2 show a close relation between the $P(sprox, 84)$ maxima periods and minimum
sunspots periods. The stationary model predicts minima in 1880 and 1960,
which is seen in the TSI-HS reconstruction (Figure 3). The Eq. 9 model iden-
tifies three additional $P(hsc, t) \leq 0$ minimum periods, which are not shown in
Table 2. These periods are (1296-1313), (1629-1656) and (1962-2002). The last
770 period had a $P(hsc, t) = -0.40$ state in 1979. The model estimates a minimum
 $P(hsc, t) \leq -0.5$ in the period (2030-2065), a grand minimum $P(hsc, t) \leq -1.0$
period (2044-2054) and a local minimum irradiation state in approximately 2050.
These estimates support the identification of Uranus, in resonance with Nep-
tune, as the major cause of TSI-HS variability.

775 The implication of this result is a chain of events between the solar inertial
motion due to the large planets and the TSI-HS variability. The SPO period
 $P(spoym, 84)$, controlled by the 84-year Uranus period may serve as a reference
for the TSI-HS variability.

4.2. TSI-LS variability

780 The TSI-LS variability is influenced by the periods from the large planets,
as shown in Table 1. The major variability is, however, influenced by the long
stationary periods $P(ls, 125)$ and $P(ls, 210)$. A stationary period is dependent
on a stationary source. The autocorrelations in Figure 8 indicate a 3/2 and
5/2 combination resonance to $P(ls, 84)$, which produce the stationary periods
785 $P(ls, 3 * 84/2 = 165)$ and $P(ls, 5 * 84/2 = 210)$. The same stationary deter-
ministic periods produce a new set of subharmonic periods $P(ls, n * 126)$ and
 $P(ls, n * 210)$ for $n = 1, 2, 3$. When $P(ls, 125)$ and $P(ls, 210)$ are related to
the stationary Uranus period $P(U, 84.02)$, they will produce a set of subhar-

monic stationary periods. The period $P(ls, 3 * 84/2 = 126.03)$ will produce
790 the subharmonic periods $P(ls, 2 * 126.03 = 252.06)$, $P(ls, 3 * 126.03 = 378.09)$,
 $P(ls, 4 * 126.03 = 504.12)$, $P(ls, 5 * 126.03 = 630.15)$ and $P(ls, 6 * 126.03 =$
 $756.18)$. The period $P(ls, 5 * 84/2 = 210.05)$ will produce the subharmonic pe-
riods $P(ls, 2 * 210.05 = 420.1)$ and $P(ls, 3 * 210.05 = 630.15)$, which indicate
that $P(ls, 126.03)$ and $P(ls, 210.05)$ have a coincidence resonance in periods of
795 approximately 630 years (Nayfeh & Mook, 2004; Ghilea, 2014).

The TSI-LS data series is reconstructed by Velasco Herrera et al. (2015), who
performed a wavelet analysis of their TSI-PMOD and TSI-ACCRIM reconstruc-
tions for the years 1000-2100 and discovered periods of 11 ± 3 , 60 ± 20 , 120 ± 30
and 240 ± 40 years. They interpret the 11-year period as the Schwabe cycle
800 and the 60-year period as the Yoshimura-Gleissberg cycle, which is associated
with solar barycentric motion. The 120 years period they associated with solar
magnetic activity (Velasco Herrera, 2013), and the 240-year period was asso-
ciated with barycentric motion as discovered by Jose (1965). They concluded
that the negative phase of the 120-year period coincides with the grand minima,
805 the positive phase of the 120-year period coincides with the grand maxima. The
next minimum should appear between 2010 and 2070 according to this inter-
pretation. Long periods were also identified by McCracken et al. (2014), who
analyzed ^{10}Be from cosmic ray variation over the past 9400 years by a Fourier
spectrum analysis and identified three related periods (65 and 130), (75 and
810 150), and (104 and 208) and the periods 350, 510 and 708 years. The identified
210-year period is known as the 210-year de Vries/Suess period. Suess (1980)
identified a stationary period of approximately 210 years in the radiocarbon
dating of pine tree rings of the last 8000 years.

The identified periods in this investigation support the study by Suess (1980);
815 Velasco Herrera et al. (2015) and McCracken et al. (2014). The new informa-
tion reveals that all long periods in the TSI-LS variability are traced to the
deterministic Uranus period $P(Uranus, 84.02)$. This study confirms that the
TSI-LS variability is dominated by deterministic periods and explains why the
identified periods from Suess (1980) and McCracken et al. (2014) are found in

820 series of 8000 and 9400 years long.

An identification stationary periods in TSI variability can provide information about future irradiation variability and expected long-term climate variation. The computed minima from the deterministic model (Eq. 13) show a close relation between the solar grand minimum periods and the computed minimum
825 periods from the model (Table 2). From this deterministic model, we may expect a new TSI minimum $P(lsc, t) \leq -0.5$ for the period 2040 – 2080, a Dalton state level $P(lsc, t) \leq -0.7$ in the time-period 2048 – 2068 and a minimum state $P(lsc, t) = -0.9$ at approximately 2060.

4.3. Sunspot variability

830 A study of the sunspot data series from 1611 identified the first dominant periods $P(sn, 11)$, $P(sn, 55)$, $P(sn, 110)$ and $P(sn, 210)$, as shown in Table 1. The period $P(sn, 11)$ is a mean estimate from a time-variant phase. The wavelet spectrum in Figure 11 shows that the period $P(sn, 55)$ has a time variant amplitude that is controlled by the period $P(sn, 110)$. The stationary first pe-
835 riod $P(sn, 11)$ is related to the Jupiter period $P(J, 11.862)$ and produces the subharmonic periods $P(sn, 5 * 11.862 = 59.31)$, $P(sn, 2 * 59.31 = 118.62)$ and $P(sn, 4 * 59.31 = 237.24)$.

The periods have a combination resonance to the Uranus period $P(U, 84.02)$. The autocorrelation spectrum in Figure 12 shows that the period $P(sn, 55)$ has
840 a 2/3 combination resonance to the period $P(sn, 84)$. This finding indicates that the identified period $P(sn, 55)$ is a stationary period that is controlled by the Uranus period $P(U, 84.02)$ from the 2/3 relation $2 * 84.02/3 = 56.01$ years. This first stationary period is expected to produce a new set of subharmonic periods of approximately $2 * 56 = 112$ and $4 * 56 = 224$ years. The identified period
845 $P(sn, 210)$ has a 5/2 combination resonance to the Uranus period $P(U, 84.02)$ by the relation $5 * 84.02/2 = 210.05$ years. Table 1 shows a close relation between the identified TSI period $P(hs, 11)$, $P(ls, 11)$, the sunspots period $P(sn, 11)$ and the Jupiter period $P(J, 11.862)$. This study has demonstrated that the Uranus period $P(U, 84.02)$ introduces a deterministic TSI period of approximately $5 *$

850 $84/2 = 210.05$ years, a deterministic sunspots period of approximately $4(2 * 84.02/3) = 224.05$ years and a mean coincidence period of 217 years.

The sunspot data series has been investigated for decades. Schwabe (1844) proposed Jupiter as a source for $P(sn, 11)$, and Ljungman (1879) presented the theory that the long-term herring biomass fluctuation was related to a 111-
855 year sunspot cycle. The 210-year de Vries/Suess period is related to a climate cycle (Suess, 1980). The new information from this study is that the 210-year de Vries/Suess period, which is identified as deterministic period in the TSI-LS and the sunspots data series, has its minimum at a phase difference of $0.7\pi/2(\text{rad/year})$ from the SPOx maximum in 1797, which coincide with Uranus
860 perigel. This shows that they are controlled by the same 84-year Uranus period,

This study shows that solar variability and TSI variability have deterministic coincidence periods of approximately 11 and 210-220 years. The deterministic model of the solar variability indicates that we may expect a new sunspot solar variability minimum $P(snc, t) \leq -0.5$ in the period from approximately 2025
865 to 2050, a Dalton level minimum $P(snc, t) \leq -0.7$ in the period from approximately 2030 to 2040 and a minimum state $P(snc, t) = -0.84$ approximately at the year 2035.

4.4. Possible explanation

This study of long solar variable data series has identified a deterministic
870 relation among TSI variability, sunspot variability, the solar position oscillation and the periods from the four large planets. In this chain of events, we may understand the solar dynamo oscillation as a coupled oscillator, forced by the oscillating gravity between the Sun and the large planets.

The study of the solar position oscillation shows that the 84-year Uranus
875 period $P(spox, 84)$ may serve as a reference for the forced gravity oscillation influence on the solar dynamo. The real SPO gravity influence on the solar dynamo is more complex. A mutual gravity oscillation exists between four large planets and the solar position oscillation that controls the angular momentum on the solar dynamo (Sharp, 2013).

880 Since the direct gravitational effect is small (Scafetta, 2012), an amplification
mechanism is necessary to produce the TSI variations. Proposed mechanisms
are a nonspherical shape of the tacholine (Abreu et al., 2008): the two meridional
circulating magnetic waves (Shepherd et al., 2014; Zharkova et al., 2015); the
tidal massage of the solar center resulting in greater nuclear energy production
885 (Scafetta, 2012); movement of elements near the center of the Sun (Wolf &
Patrone, 2010; Cionco & Soon, 2015) or reconnection of magnetic field lines
which create magnetic bubbles (Granpierre, 2015). A sudden loss of angular
momentum from solar rotation to solar and planetary orbit may cause variation
in differential rotation that modulates the dynamo, which generates a magnetic
890 field and sunspot variations (Blizzard, 1981). Transfer of angular momentum
between the rotation of the Sun and the orbit of the planets is possible because
of the wobble of the Sun. The axis of rotation is tilted with respect to the axes
of the orbital plane, and the shape of the Sun is elliptical in the polar directions.
Since the Earth also moves inside the solar wind, modulation of the solar wind
895 by the four large planets may also be directly felt by the Earth, in addition
to exchange of angular momentum resulting in faster or slower rotation, which
modulates the Earths climate (Mörner, 2010).

Other studies have identified stationary periods in the solar dynamo. Duhau
& De Jager (2008) analyzed the variation of the solar-dynamo magnetic-field
900 since 800 and identified periods of approximately 11, 22, 88 and 208 years.
Shepherd et al. (2014) and Zharkova et al. (2015) have identified two dynamo
waves that show periods of 320 - 400 years, with an amplitude modulation in
the range of 20 - 24 years. These periods are similar to some of the identified
periods in Table 1. The new information from this study is that the identified
905 solar dynamo periods have a deterministic relation to the stationary periods
from the four large planets, the TSI variability and the sunspot variability.
The stationary solar dynamic periods explains why the 125-year TSI-LS period
produces a subharmonic period of approximately $3 * 125$ or 375 years.

5. Conclusions

910 A better understanding of the deterministic properties of the TSI variability
is critical for understanding the cause of irradiation variability and how the TSI
irradiation will contribute to the natural climate variation on the Earth. In this
study, we have identified stationary periods in the TSI-HS data series from 1700-
2013, in the TSI-LS data series from 1000-2100 and in the sunspots data series
915 from 1610-2015. The identified stationary periods are related to the SPO and the
periods from the four large planets. The results show that the TSI and sunspot
data series variability have stationary oscillating periods that is controlled by
the gravity from the large planets Jupiter, Saturn, Uranus and Neptune. The
identified periodic relation between the solar system oscillation and the TSI
920 variability, indicates a chain of events between the solar system oscillation and
the TSI variability. A possible chain of events is that the oscillating gravity
between the Sun and the large planets influences the solar dynamo oscillation,
which produces the TSI variability and the sunspot variability.

The study demonstrates that the major TSI variability and sunspot variabil-
925 ity are controlled by the 11-year Jupiter period and the 84-year Uranus period.
The TSI data series from 1700 has a variability that is controlled by the 11-year
Jupiter period and the 84-year Uranus period. The TSI data series from 1000
has a stationary dominant period of approximately 125 years, which is con-
trolled by a $3/2$ resonance to the 84-year Uranus period, and a 210-year period
930 by a $5/2$ resonances to the 84-year Uranus period. The stationary periods of
approximately 125 and 210 years introduce a new set of deterministic subhar-
monic periods. The study confirms the deterministic relation between 210-year
variability and TSI variability, which is known as the 210-year de Vries/Suess
period (Suess, 1980).

935 The identified stationary periods in TSI variability and sunspot variability
are transformed to deterministic models of TSI oscillation and sunspot oscilla-
tion. The close relation between the computed minima and the known mini-
mum periods since 1000 confirms the identified periods from this study. The

deterministic model of sunspots and TSI computes a new Dalton-type sunspot
940 minimum from 2025 to 2050 and a new Dalton-period-type TSI minimum from
approximately 2040 to 2065.

Acknowledgements

We thank N. Scafetta and V. M. Velasco Herrera for providing the data sets
for TSI we have used in this investigation. We also thank an anonymous referee
945 for valuable suggestions, helping us to improve the manuscript.

References

- Abreu, J.A., Beer, J., Steinhilber, F., Tobias, S.M. and Weiss, N.O., 2008, For
how long will the current grand maximum of solar activity persist?. *Geophys.*
Res. Lett., 35, L20109
- 950 Blizard, J.B., 1981, Solar Motion and Solar Activity, *Bull. Am. Astron. Soc*, 13,
876
- Charbonneau, P. 2010, Dynamo Model of the Solar Cycle, *Living Rev. Sol.*
Phys.,7,3, www.livingreviews.org/lrsp-2010-3
- Charvátová & Hejda, 2014, Responses of the basic cycles of 178.7 and 2402 year
955 in solar-terrestrial phenomena during the Holocene, *Pattern Recognit. Phys.*
2, 21-26.
- Cionco, R.G. and Soon, W., 2015, A phenomenological study of the timing of
solar activity minima of the last millennium through a physical modeling of
the Sun-Planets Interaction, *New Astron.*, 34, 164-171.
- 960 Clette, F., Svalgaard, L., Vaquero, J. M, and Cliver, E.W., 2014, Revisiting the
Sunspot Number, in *The Solar Activity Cycle*, V 53 Space Sciences Series of
ISSSI pp 35-103.
- Daubechies I. 1992. Ten lectures of wavelet. *SIAM J. Math. Anal.* 24:499-519.

- De Jager, C. and Duhau, S., 2011, The Variable Solar Dynamo and the Forecast
965 of Solar Activity; Influence on Terrestrial Surface Temperature, in Global
warming in the 21st Century, J.M.Cossia (ed), ISBN978-1-61728-980-4. Nova
Science Publishers, Inc.
- Duhau S. and De Jager C., 2008. The Solar Dynamo and Its Phase Transition
during the Last Millennium. *Sol. Phys.*, 250: 1-15.
- 970 Eddy, J.A., 1983, The Maunder Minimum A reappraisal, *Sol. Phys.*, 89, 195-
207, DOI: 10007/BF00211962.
- Eddy, J.A., 1976, The Maunder Minimum, *Science*, 192,1189-1202
- Fairbridge, R.W. and Shirley, J.H., 198, *Sol. Phys.*, 110, 191-220.
- Foukal, P., Bernasconi, P. & Fröhlich, C., 2009, Recent anomalous TSI decrease
975 not due to low polar facula and network areas: Time to broaden our view on
solar luminosity variation?, *Bull. Am. Astron. Soc.*, 41,827.
- Frölich, C. & Lean, J., 1998, The Sun's Total Irradiance: Cycles, Trends and
Related Climate Change Uncertainties since 1976, *Geophys. Res. Lett.*, 25,
no 23, 4377-4380
- 980 Ghilea, M. C.,2014. Statistical distributions of mean motion resonances and
near-resonances in multiplanetary systems). arXiv:14102478G
- Gleissberg, W., 1965,The eighty-year solar cycle in auroral frequency numbers,
J. Br. Astron. Assoc., 75, 227231.
- Gleissberg, W., 1958, The eighty-year sunspot cycle, *J. Br. Astron. Assoc.*, 68,
985 148152.
- Granpierre, A., 2015, The origin of solar activity: Local thermonuclear runaways
in hot bubbles and their triggers, In: *Planetary influence on the Sun and the
Earth, and a modern book-burning*, Ed: N.-A. Mörner, Nova publ, ISBN
978-1-63482-837-6, p.91-108.

- 990 Granpierre, A., 1990, How is the Sun working?, *Sol. Phys.*, 128, 3-6.
- Granpierre, A., 1996, On the origin of solar periodicity. *Astrophys. Space Sci.* 243,393-400.
- Hassan, D. et al., 2016, Sunspots and ENSO relationship using Markov method, *J. Atmos. Sol. Terr. Phys.*, 137, 53-57, [dx.doi.org/10.1016/j.jastp.2015.11.017](https://doi.org/10.1016/j.jastp.2015.11.017).
- 995 Hathaway, D.H., 2015, The Solar Cycle, *Living Rev. Sol. Phys.*, 12,(4).
- Hoyt, D. V., and Schatten K. H. 1993. A Discussion of Plausible Solar Irradiance Variations, 1700-1992. *J. Geophys. Res.*, 98, 18895-18906.
- Hoyt, D. V., Schatten, K.H., and Nesme-Ribes, E., 1994, The one hundredth year of Rudolf Wolfs death: Do we have the correct reconstruction of solar activity?, *Geophys. Res. Lett.*, 21, 2067-2070.
- 1000 Hoyt, D.V. and Schatten, K.H., 1998a, Group Sunspot Numbers: A New Solar Activity Reconstruction, *Sol. Phys.*, 179, 189-219.
- Hoyt, D.V. and Schatten, K.H., 1998b, Group Sunspot Numbers: A New Solar Activity Reconstruction, *Sol. Phys.*, 181, 491-512.
- 1005 Hung, C.-C., 2007, Apparent relations between solar activity and solar tides caused by the planets, NASA/TM-2007-214817. Technical Memorandum.
- Jose, P. D. 1965, Sun's motion and sunspots, *Astron. J.*, 70, 193-200, 1965.
- Ljungman, A. V. 1879. Bidrag till lösningen af frågan om de stora sillfiskenas sekulära periodisitet. *Tidskrift for Fiskeri*, 5: 257-268. (In Swedish).
- 1010 Ljungquist, F.C., 2010, A new reconstruction of temperature variability in the extra-tropical Northern hemisphere during the last two millennia, *Geogra. Ann.*, 92 A(3) 339-351.
- Matlab. 2015. Matlab. Wavelet Toolbox. Users Guide. The Math Works Inc.
- Maunder, E.W., 1890, Professor Spoerers Researches on Sun-spots, *MNRAS*, 50, 251-252.
- 1015

- McCracken, K.G., Beer, J., and Steinhilber, F., 2014. Evidence for Planetary Forcing of the Cosmic Ray Intensity and Solar Activity Throughout the Past 9400 Years., *Sol. Phys.*, 289,3207-3229, doi:10.1007/s11207-014-0510-1
- Mörner, N.-A., 2010, Solar Minima, Earth's rotation and Little Ice Ages in the past and in the future The North Atlantic-European case, *Global Planet. Change*, 72, 282-293, doi:10.1016/j.gloplacha.2010.01.004.
- Mörner, N.-A., Scafetta, N. & Solheim, J.-E., 2015, The January 7 giant solar flare, The simultaneous triple planetary conjunction and additional records at Tromsø, Norway, In: *Planetary influence on the Sun and the Earth, and a modern book-burning*, Ed: N.-A. Mörner, Nova publ, ISBN 978-1-63482-837-6, p.33-38.
- Nayfeh A. H. and Mook D. T., 2004. *Nonlinear Oscillations*. WILEY-VCH Verlag GmbH & Co. KGaA, Weinheim. ISBN-10:0-471-12142-8.
- Ogurtsov, M.G., Nagovitsy, A., Kocharov, G.E. and Jungner, H., 2002, Long-period cycles of the Sun's activity recorded in direct solar data and proxies, *Sol. Phys.*, 211,371-394.
- Peristykh, A.N. and Damon, P.E., 2003, Persistence of the Gleissberg 88-year solar cycle over the last ~12,000 years: Evidence from cosmogenic isotopes, *J. Geophys. Res. Space Phys.*, 108,A1,pp.SSH 1-1, CiteID 1003, doi: 10.1029/2002JA009390
- Scafetta N., 2014. Discussion of the spectral coherence between planetary, solar and climate oscillations: a reply to some critiques, *Astrophys. Space Sci*, 354(2), 275-299, doi: 10.1007/s10509-014-2111-8
- Scafetta N. and Willson R.C., 2014, ACRIM total solar irradiance satellite composite validation versus TSI proxy models. *Astrophys. Space Sci.*, 350(2), 421-442. DOI 10.1007/s10509-013-1775-9.

- Scafetta, N. 2012, Does the Sun work as a nuclear fusion amplifier of planetary tidal forcing? A proposal for a physical mechanism based on the mass-luminosity relation, *J. Atmos. Sol. Terr. Phys.* 81-82, 27-40.
- 1045 Schwabe, H., 1844, *Sonnen-Beobachtungen im Jahre 1843*, *Astron. Nachr.* 21, (495), 233-236.
- Sharp, G.J., 2013, Are Uranus & Neptune Responsible for Solar Grand Minima and Solar Cycle Modulation?, *Int. J. Ast. & Astrophys.*, 3, 260-273, dx.doi.org/10.4236/ijaa.2013.33031.
- 1050 Shepherd, S. J., Zharkov, S.I. and Zharkova, V.V. 2014, Prediction of Solar Activity from Solar Background Magnetic Field Variations in Cycles 21-23. *ApJ*. 795(1), article id. 46,8 pp, doi: 10.1088/0004-637X/795/1/46
- Solanki, S.K., Usoskin, I.G., Kromer, B., Schssler, M. and Beer, J.. 2004, Unusual activity of the Sun during recent decades compared to the previous 11,000 years, *Nature*, 431, 1084-1087.
- 1055
- Soon, W, Connolly, R. and Connolly, M., 2015, Re-evaluating the role of solar variability on Northern Hemisphere temperature trends since the 19th century, *Earth-Sci. Rev.*, 150, 409.
- Suess, H.E., 1980, The Radiocarbon Record in Tree Rings of the Last 8000 Years, *Proc. of the 10th international Conference on Radiocarbon Dating, Bern and Heidelberg 1979*, *Radiocarbon*, 22, 200-209.
- 1060
- Usoskin, I.G., et al. 2014, Evidence for distinct modes of solar activity, *A& A*, 562, L10, DOI: 10.1051/0004-6361/201423391.
- Usoskin, I. G., 2013, A History of Solar Activity over Millennia, *Living Rev. Solar Phys.*, 10,1. URL(accessed 2014, 0530): <http://www.livingreviews.org/lrsp-2013-1>
- 1065
- Usoskin, I.G., Solanki, S.K. and Kovaltsov, G.A., 2007, Grand minima and maxima of solar activity: new observational constraints *A& A*, 471, 301-309.

- 1070 Usoskin, I.G., Solanki, S.K., Schüssler, M., Mursula, K. and Alanko, K., 2003, Millennium-Scale Sunspot Number Reconstruction: Evidence for an Unusually Active Sun since the 1940s, *Phys. Rev. Lett.*, 91, 211101.
- Velasco Herrera, V.M, Mendoza, B. and Velasco Herrera, G., 2015, Reconstruction and prediction of the total solar irradiance: From the Medieval Warm Period to the 21st century, *New Astron.*, 34, 221-233.
- 1075 Velasco Herrera, V.M., 2013, Homage to the Discovery of Cosmic Rays, the Meson-Muon and Solar Cosmic Rays, *Nova publ.*, Jorge A., Perez-Peraza (Eds), chap. 15, 469.
- Velasco, V.M. and Mendoza, B., 2008, Assessing the relationship between solar activity and some large scale climatic phenomena, *Adv. Space Res.*, 42, 866-1080 878, DOI: 10.1016/j.asr.2007.05.050
- Willson, R.C., 2014, ACRIM3 and the Total Solar Irradiance database, *Astrophys. Space Sci*, 352(2), 341-352, doi: 10.1007/s 10509-014-1961-4
- Wilson, I.R.G., 2013, The Venus-Earth-Jupiter spin-orbit coupling model, *Pattern Recognit. Phys.*, 1, 147-158, doi:10.5194/prp-1-147-2013-
- 1085 Wolf, C.L. and O'Donovan, A.E., 2007, Coupled groups of g-modes in a Sun with a mixed core, *ApJ*. 661, 568-585.
- Wolf R., 1859, Extract of a Letter to Mr. Carrington, *MNRAS*, 19, 85-86.
- Wolf, C.I. and Patrone P. N., A New Way that Planets Can Affect the Sun, 2010, *Sol. Phys*, 266, 227-246, DOI 10.1007/s11207-0101-9628-y.
- 1090 Wolf, R., 1861, Abstract of his latest Results, *MNRAS*, 21, 77-78
- Zhao, J., Bogart, R.S., Kosovichev, A.G., Duvall, T.L. Jr., & Hartlep, T., 2013, Detection of Equatorward Meridional Flow and Evidence of Double-cell Meridional Circulation inside the Sun, *ApJ*, 774, L29.

Zharkova, V.V., Shepherd, S.J., Popova, E. and Zharkov, S.I.,2015, Heartbeat
1095 of the Sun from Principal Component Analysis and prediction of solar activity
on a millennium timescale, www.nature.com/Scientific reports, 5:15689, DOI:
10.1038/srep1569.

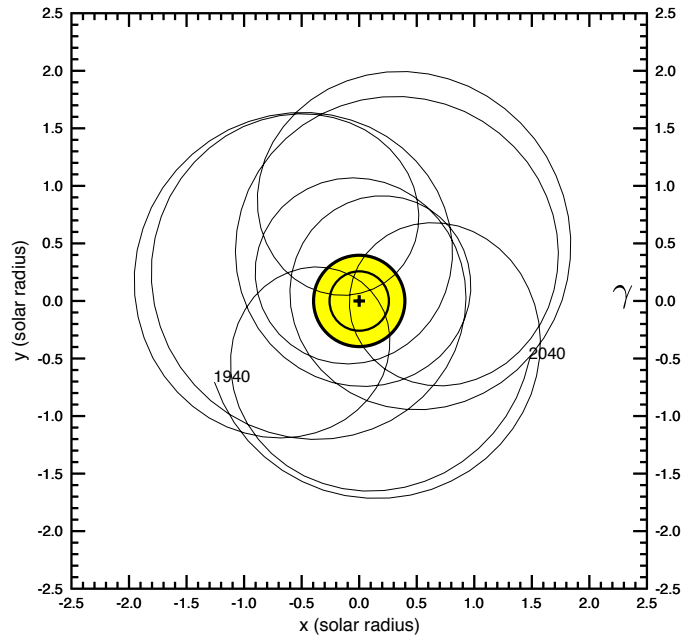


Figure 1: Orbit of the solar center with respect to the solar system barycenter (SSB) (+) for the period 1940–2040 in the ecliptic plane that is defined in the direction of the Earth vernal equinox (Υ). The outer yellow circle represents the diameter of the Sun, and the inner circle at radius $0.65r_{sun}$ represents a shell where the potential energy (PE) of the solar radiative zone can be affected if the solar center moves closer to the SSB (Cionco & Soon, 2015).

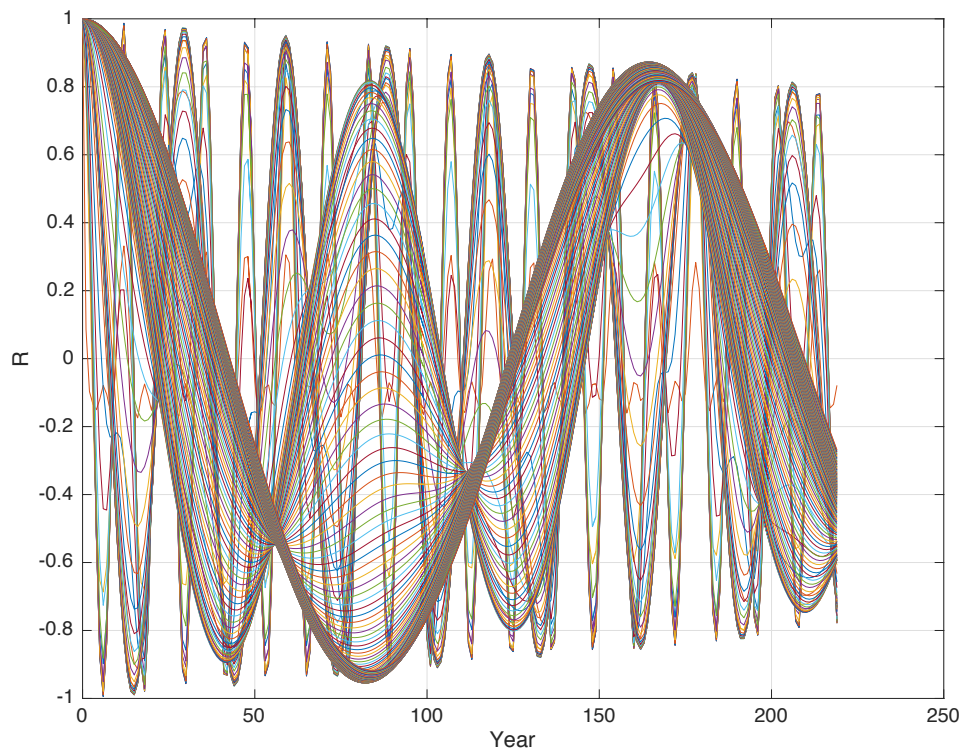


Figure 2: Autocorrelation spectrum $R_{spoy}(s, m)$ of Sun position oscillation ($SPOy$) wavelet spectrum. Each colored line represents a single autocorrelation.

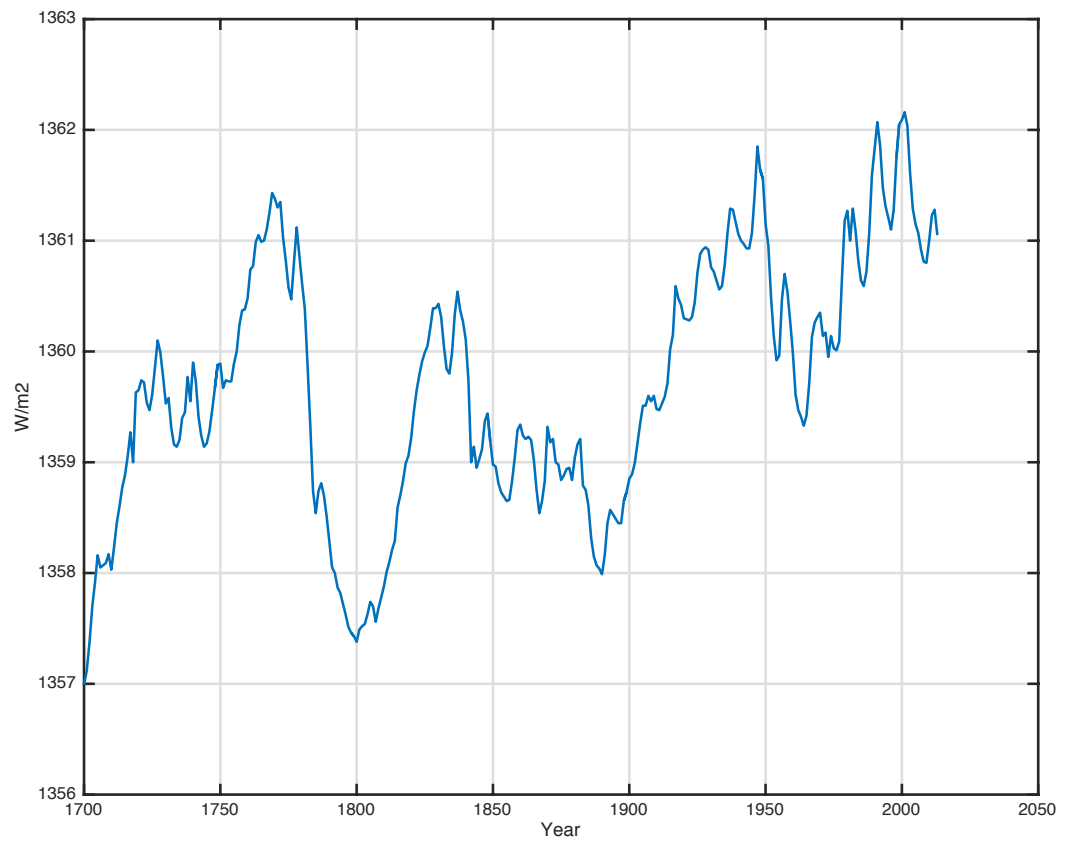


Figure 3: TSI-HS total solar irradiance from 1700 to 2013 ((Scafetta & Willson, 2014).

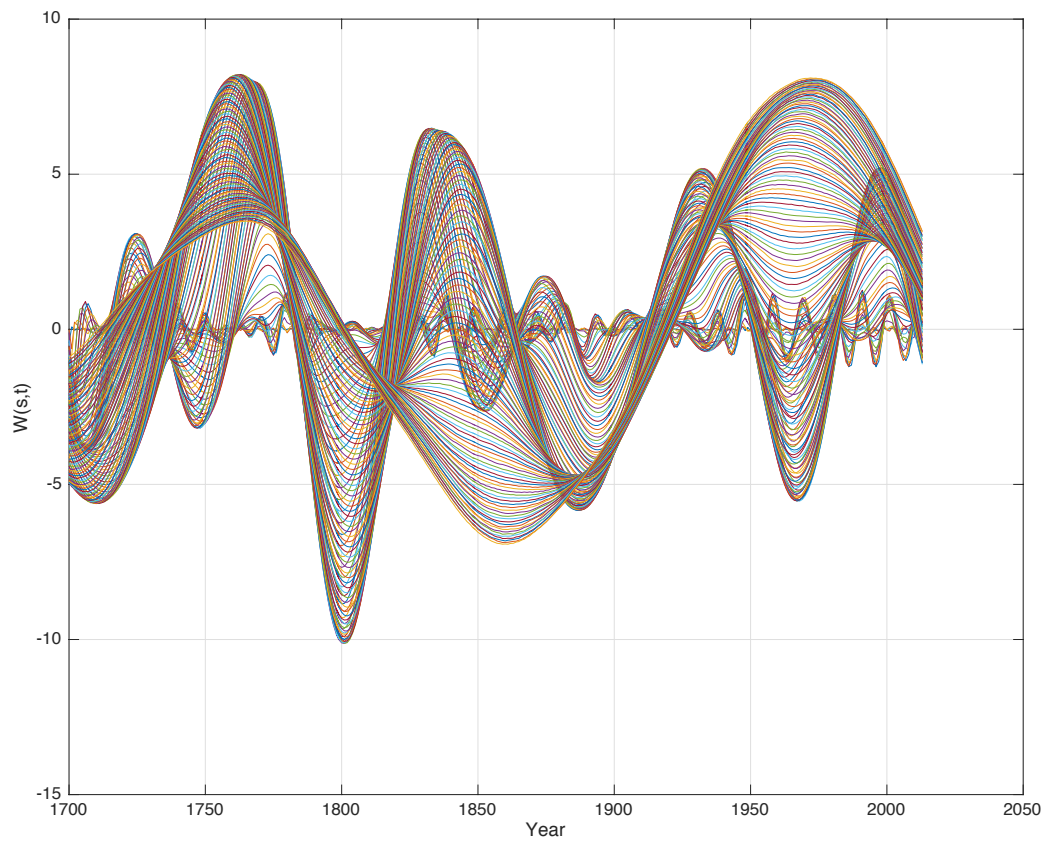


Figure 4: Wavelet spectrum $W_h s(s, t)$ of the TSI-HS data series, for $s = 1 \dots 0.6N$.

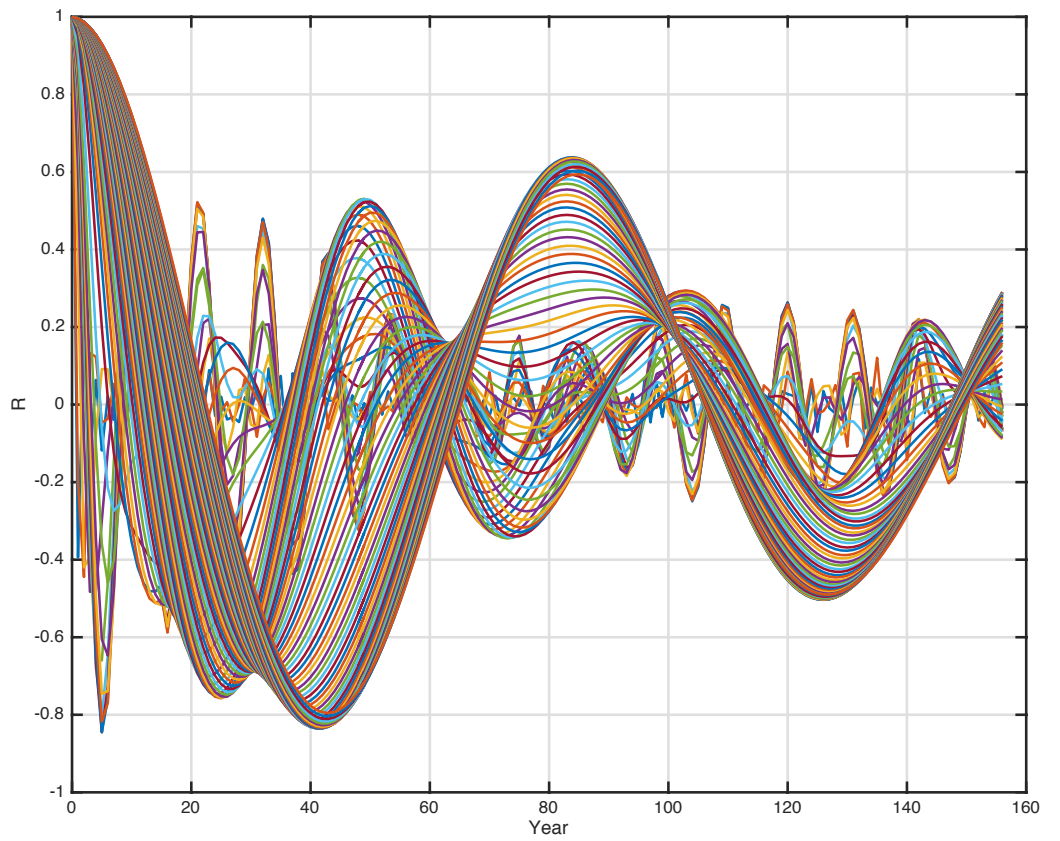


Figure 5: Autocorrelation spectrum $Rhs(s, m)$ of the TSI-HS wavelet spectrum $Whs(s, t)$ for $s = 1 \dots 190$ and $m = 0 \dots 160$.

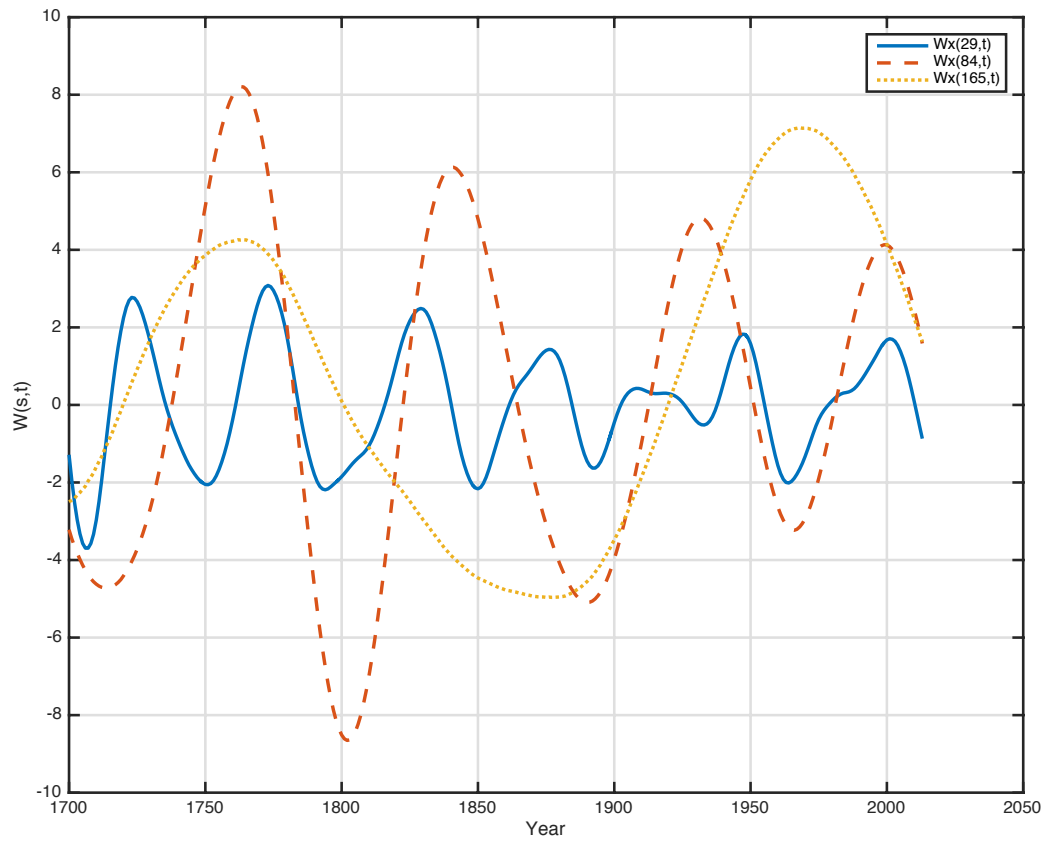


Figure 6: The identified stationary wavelet periods $W_{hs}(49, t)$, $W_{hs}(86, t)$ and $W_{hs}(165, t)$ from the TSI-HS wavelet spectrum $W_{hs}(s, t)$.

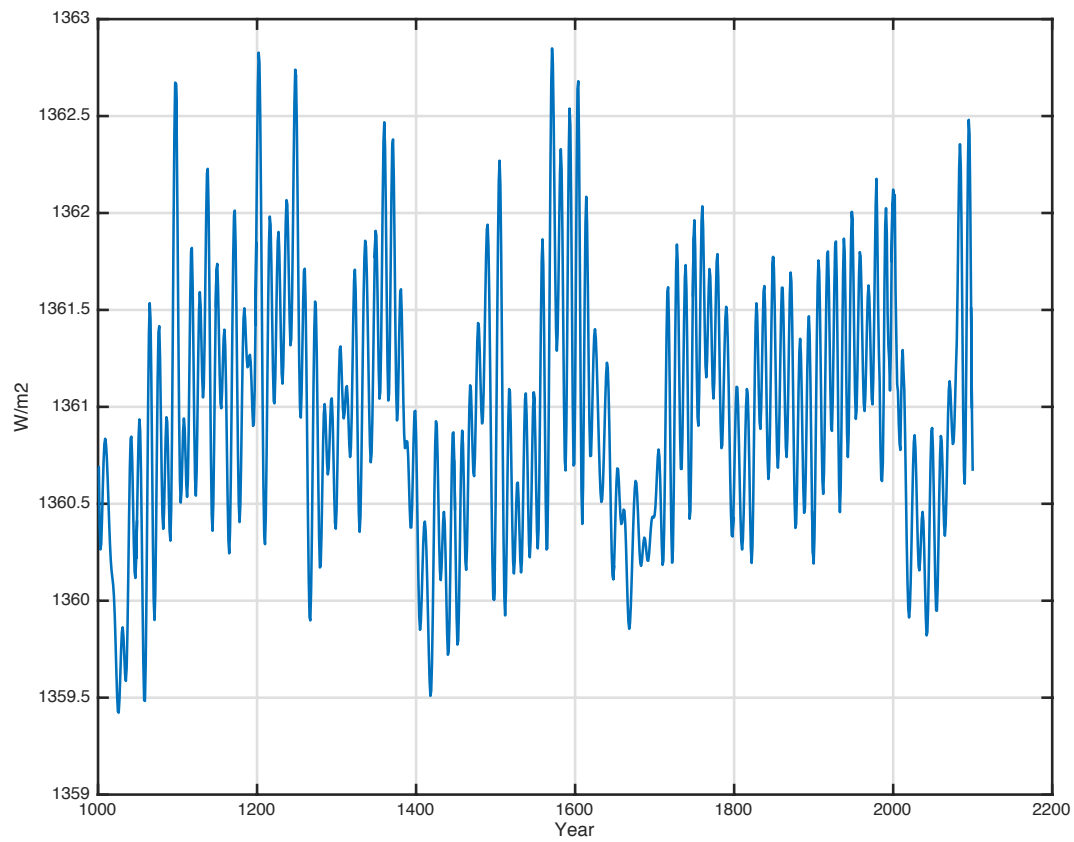


Figure 7: TSI-LS data series from 1000 to 2100 Velasco Herrera et al. (2015).

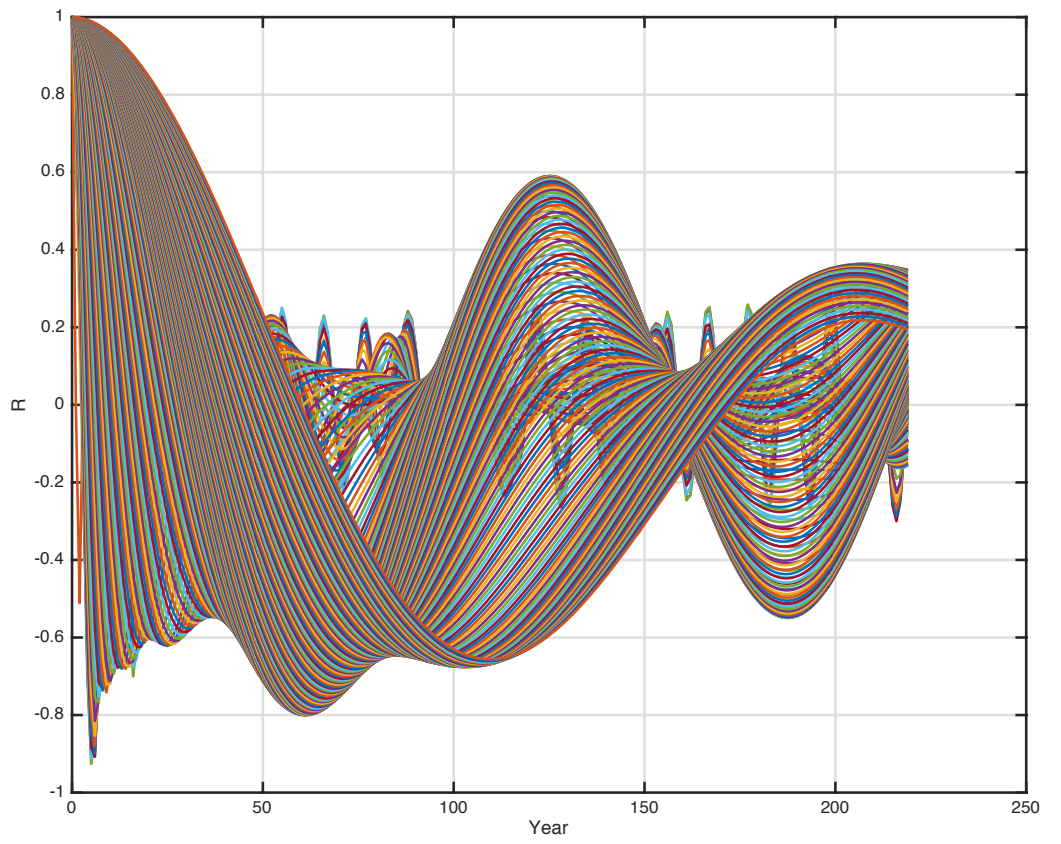


Figure 8: Computed autocorrelation $Rls(s, m)$ of the TSI-LS wavelet spectrum $Wls(s, t)$.

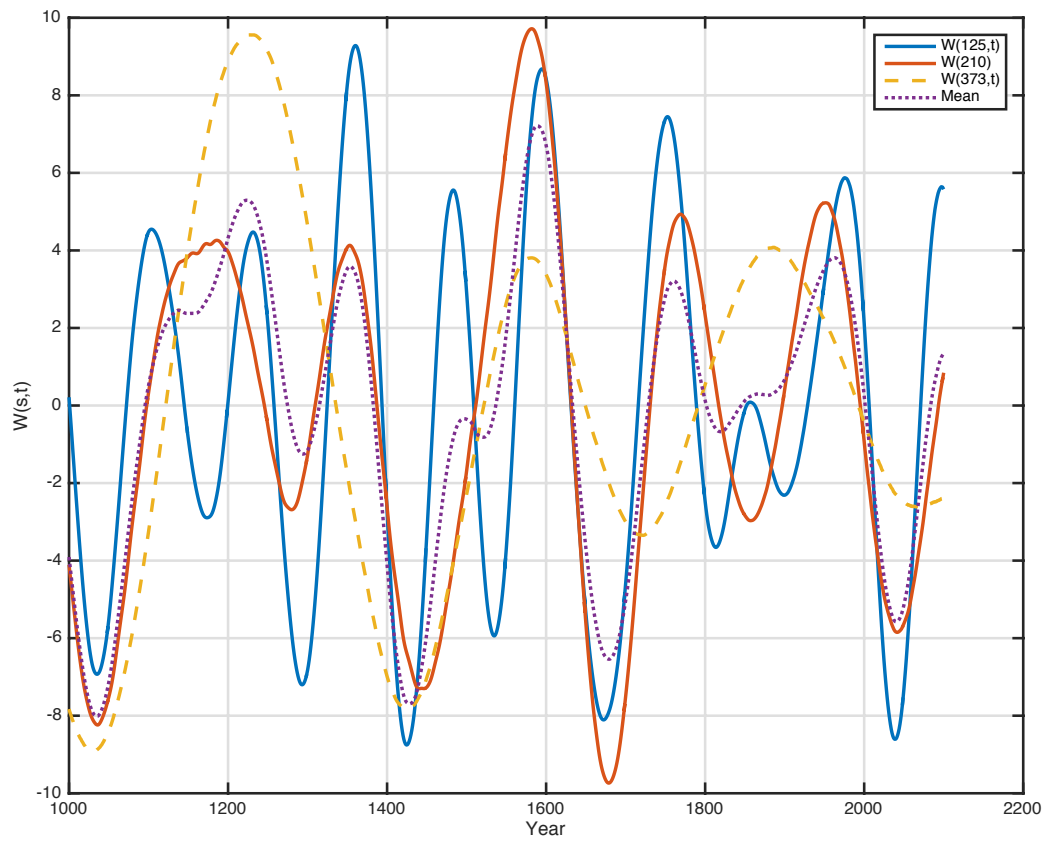


Figure 9: The identified long stationary wavelet periods $Wls(125, t), Wls(210, t)Wls(373, t)$ and the period mean value

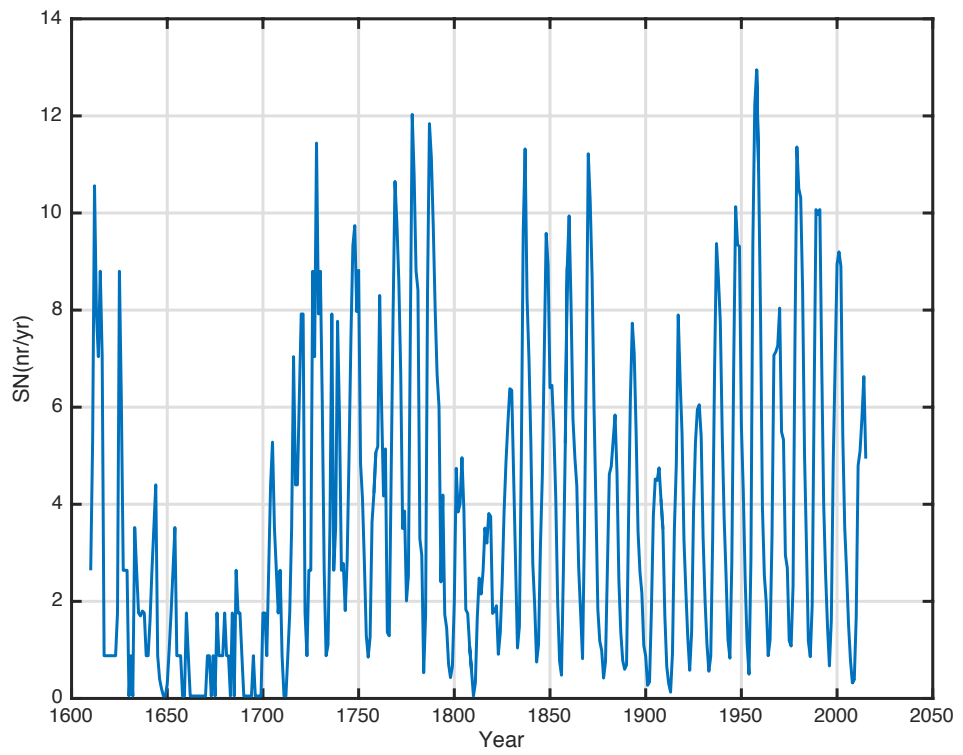


Figure 10: Solar variability represented by the yearly average group sunspot number series $SN(t)$, estimated from 1610 to 2015 (SILSO data/image, Royal Observatory of Belgium, Brussels)

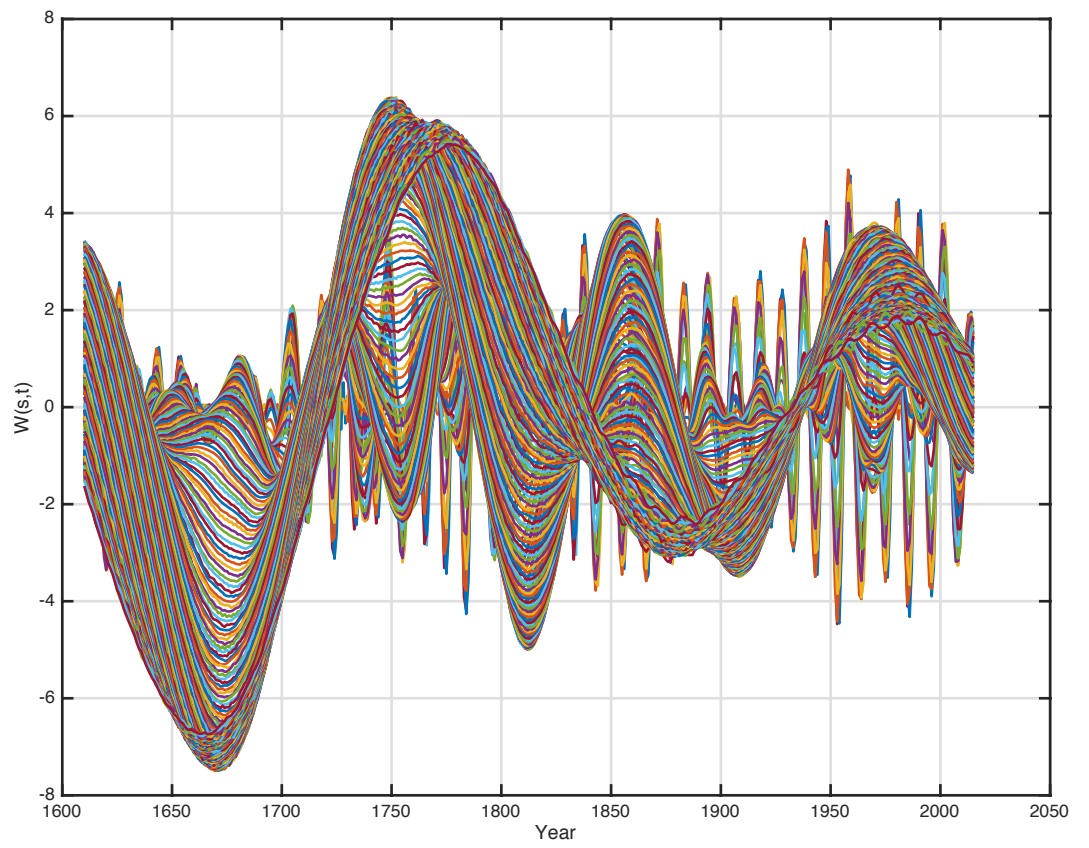


Figure 11: Wavelet spectrum $Wsn(s,t)$ of the sunspot data series $SN(t)$.

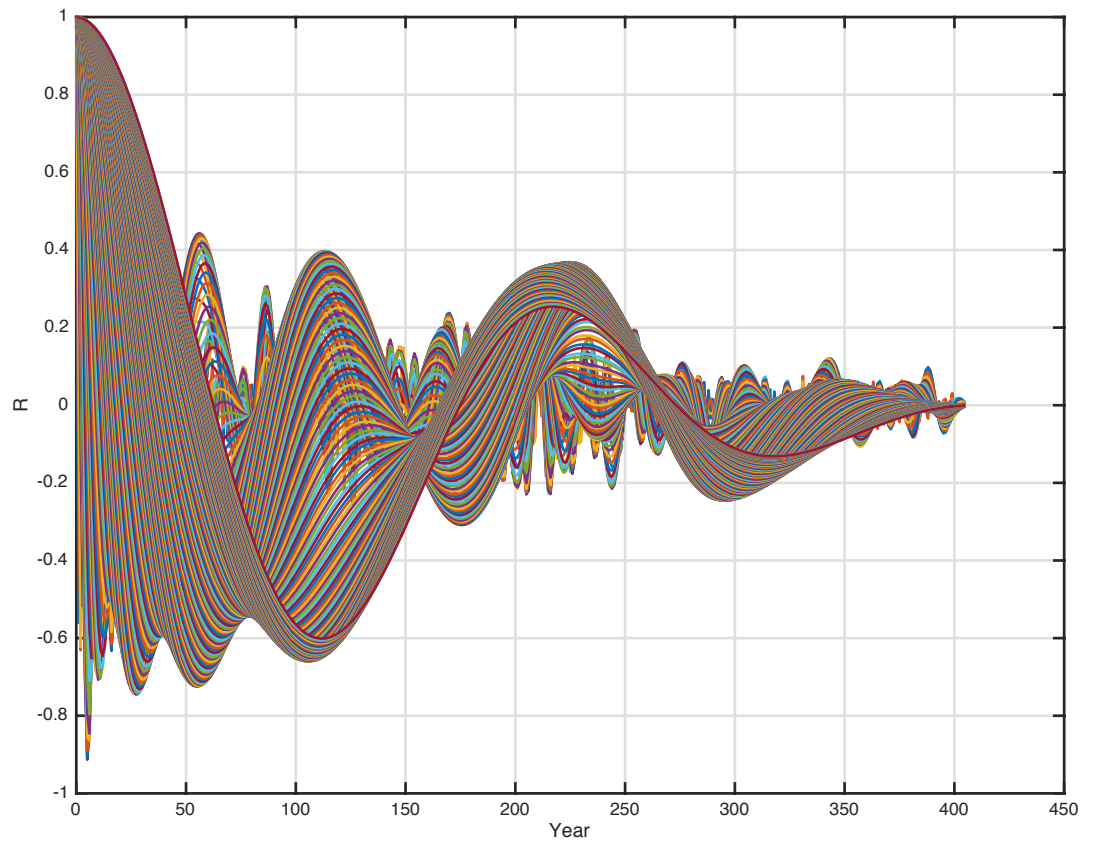


Figure 12: Computed set of autocorrelations $Rsn(s, m)$ of the sunspot wavelet spectrum $Wsn(s, t)$.